Assessment of hip deformities during childhood: a combined approach of Machine Learning and Finite Element Analysis

Klara Eriksson & Jonna Fahrman

Lund, June 2022

LUND
UNIVERSITY

Master's Thesis in
Biomedical Engineering

Faculty of Engineering, LTH
Department of Biomedical Engineering

Main supervisor: Lorenzo Grassi
Co-supervisors: Hector Dejea, Gustavo Orozco
& Hanna Isaksson

Title
Assessment of hip deformities during childhood: a combined approach of Machine Learning and Finite Element Analysis

Author
Klara Eriksson & Jonna Fahrman

Figures
Created by the authors unless otherwise stated

Lunds Universitet
Institutionen för biomedicinsk teknik
Box 118
SE-221 00 Lund
Sverige

E-husets tryckeri
Lund 2022

Acknowledgements

We would like to start off with a big thank you to our supervisors. To Lorenzo Grassi, for being available with guidance whenever we needed it in spite of parental leave. To Hector Dejea, for great input on our work and for always showing a great interest in what we do. To Gustavo Orozco, for your time and patience, as well as for sharing your Abaqus expertise and always being available to help us with the FE models. To Hanna Isaksson for valuable advice along the way. And to all, thank you for dedicating your time and effort to our thesis.

Finally, to the entire division of biomechanics, thank you for making us feel welcome and included from the very start and for making us feel like a part of the group.

Abstract

Osteoarthritis is a degenerative disease that will cause pain and stiffness in the joint if not treated. One cause of early osteoarthritis in the hip joint is pediatric hip deformities. Hip deformities can occur in different stages of childhood and cause the bones to be misshapen or the hip joint to be dislocated.

This thesis aimed to build subject-specific computer models of the hip joint to find a biomechanical connection between pediatric hip deformities and osteoarthritis. The aim was approached through three main tasks:

- Automatically detect anatomical landmarks on two-dimensional X-ray images. This can be used to automate three-dimensional reconstructions of the femur.
- Predict the effects of common loading scenarios in the hip joint cartilage using subject-specific numerical models developed using X-ray Computed Tomography (CT) images. The model can later be customized to fit a reconstructed femur.
- Assess the feasibility of obtaining a three-dimensional subject-specific numerical model of the hip joint from a two-dimensional X-ray image to predict the mechanical effect of common loading scenarios in the cartilage.

For the methodology, Dual-energy X-ray Absorptiometry images of hip joints were used to evaluate and refine a machine learning based method for automatic landmark detection. Additionally, a finite element model was developed based on a CT image and it modeled one-leg-stance and walking. Finally, three-dimensional reconstructions of the femur were made based on automatically detected landmarks on two-dimensional X-ray images and used to scale the finite element model to match the size of each reconstructed femur.

Results showed that the method for automatic landmark detection was able to identify eight anatomical landmarks in the hip joint with

an average error of 0.33 mm when compared to manually annotated landmarks. The finite element model of the hip joint agreed well with literature when calculating the contact pressure in the cartilage during standing and walking. Finite element models scaled in three directions based on reconstructed femurs were able to predict hip joint cartilage mechanics.

As this project showed that the concept of creating a three-dimensional finite element model based on two-dimensional X-ray images was successful, future research should focus on automating the process further and making it applicable to children to be more clinically relevant. This could enable the possibility to gain information on how pediatric hip deformities affects the cartilage in the hip joint without additional radiation exposure.

List of acronyms & abbreviations

2D - two-dimensional

3D - three-dimensional

CNN - convolutional neural network

CT - computed tomography

DDH - developmental dysplasia of the hip

DXA - dual-energy x-ray absorptiometry

E - young's modulus

FAI - femoroacetabular impingement

FE - finite element

FEA - finite element analysis

HOG - histogram of oriented gradients

LCPD - legg-calve-perthes disease

ML - machine learning

MRI - magnetic resonance imaging

OA - osteoarthritis

oML-morph - original ML-morph

SCFE - slipped capital femoral epiphysis

sML-morph - simple ML-morph

SSAM - statistical shape and appearance model

ν - poisson's ratio

Contents

Chapter 1

Introduction

Osteoarthritis (OA) is a disease that affects millions of people all over the world and it is the most common form of arthritis [1]. One cause of osteoarthritis is hip deformities that occur during childhood [2]. Certain hip deformities occur before the child is born and others develop as the child is growing [3]. Hip dysplasia is one type of hip deformity that affects children and 3-5% of the population is affected. Hip dysplasia is a progressing condition that can cause structural damage to the hip and it is the number one cause of early osteoarthritis that occurs before 60 years of age [2]. In total, 15% of the adult population is affected by OA and it is one of the leading causes of disability in the lower extremities [4]. OA leads to degradation of the cartilage and can cause the patient pain and discomfort as well as loss of flexibility. The progression of the disease can be slowed down with treatment but as the condition is irreversible, the treatment has to start as early as possible [1].

While the initial method of examining newborns in regards to hip deformities is a physical examination, radiographs are the most used method of examination when the child is older than six months [5]. One limitation of radiographs is that even though they can show abnormalities in the joint, it is not possible to show the exact location of the irregularity or the shape of the joint. X-ray Computed Tomography (CT), a three-dimensional (3D) X-ray imaging technique, can give a better view of the tissues in the hip joint. Major downsides to capturing CT images compared to two-dimensional (2D) X-ray images are that it is more costly [6], and will subject the patient to a higher dose of radiation, something that should be particularly limited in children [7].

Since the standard procedure when evaluating hip deformities is 2D X-ray images, it would be beneficial to use the same images to model the geometry and function of the joint. One possible alternative to this is to reconstruct a 3D geometry of the hip from the 2D image. A method for reconstructing femurs based on 2D X-ray images was previously developed by Väänänen et al. [8]. The input used for the reconstruction is a Dual-energy X-ray Absorptiometry (DXA) image and corresponding anatomical landmarks. To produce reconstructed femurs based on automatically detected landmarks would make it possible to reconstruct a larger number of anatomies with minimum human interaction.

A 3D subject-specific finite element (FE) model of the hip joint can assist in understanding how the forces acting on the hip are affecting the different structures. It could then be used to determine the best route of treatment and what intervention is necessary for the patient. To make the FE models of the hip from 2D X-ray images would be beneficial as it would lower the cost [6] and the dose of ionizing radiation [7].

1.1 Aim

This thesis aimed to build subject-specific computer models of the hip joint to find a biomechanical connection between pediatric hip deformities and osteoarthritis. The aim was approached through three main tasks:

- **Automatic landmark detection**: Automatically detect anatomical landmarks on 2D X-ray images. This can be used to automate 3D reconstructions of the femur.
- **Subject-specific FE model of the hip**: Predict the effects of common loading scenarios in the hip joint cartilage using subject-specific numerical models developed using CT images. The model can later be customized to fit a reconstructed femur.
- **Reconstruction of DXA images and scaling of the FE model**: Assess the feasibility of obtaining a 3D subject-specific numerical model of the hip joint from a 2D X-ray image to predict the mechanical effect of common loading scenarios in the cartilage.

1.2 Design of the study

This master's thesis was comprised of three different sections: automatic landmark detection, subject-specific FE modeling, and one section focused on reconstructing the femur from the DXA images and scaling of the FE model. An overview of the thesis can be seen in figure 1.1.

DXA images previously annotated by Dr. Lorenzo Grassi were used as a starting point of the automatic landmark detection. ML algorithms were used and tests were performed to determine the accuracy of the predicted landmarks. The second part of the thesis used a CT image to develop a subject-specific FE model of the hip joint, modeling two common loading scenarios. The two parts were combined to reconstruct femurs based on the landmarks in the DXA images and scale the FE model to be of the same size as the reconstructed femur.

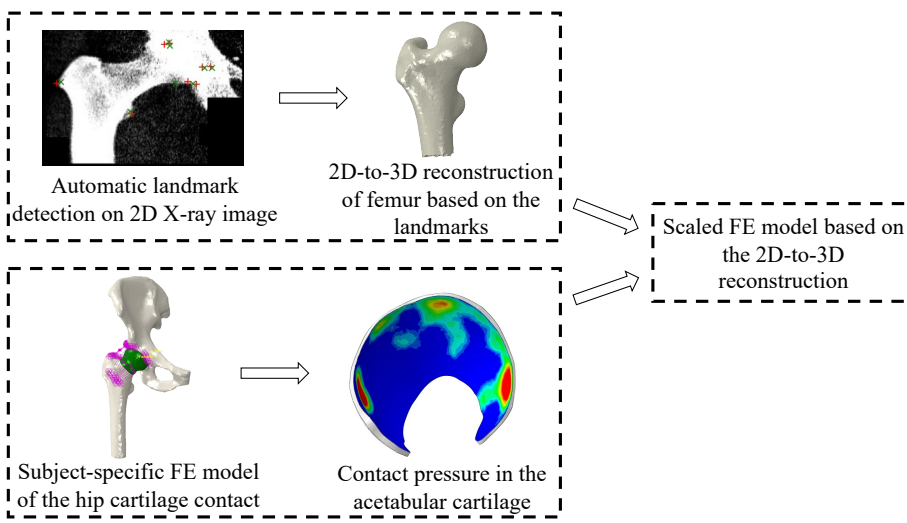

Figure 1.1: Schematic of the design of the master's thesis project.

1.3 Authors' contribution

The three parts of this thesis have been divided between the two authors. The automatic landmark detection was performed by Jonna Fahrman and the subject-specific FE model was developed by Klara Eriksson. The reconstruction and scaling was done in equal parts by both authors. Both authors have contributed equally to writing and revising

this thesis. By dividing the project into two separate parts, the authors have gained the possibility to help and assist each other in close collaboration while making the work efficient and taking advantage of their different backgrounds.

Chapter 2

Background

In this chapter, general background about the anatomy and biomechanics of the hip joint, OA progression, and typical deformities during childhood are described. The relevant theory for automatic landmark detection in DXA images and subject-specific FE modeling from clinical images is also presented.

2.1 Hip anatomy

The human hip joint is the connection between the pelvis and the femur (see figure 2.1). It is a ball (femoral head) and socket (acetabulum) joint and allows rotation in all directions. The joint is surrounded by ligaments that connect the bones and restrict movement [9]. The surface of the acetabulum and the femoral head is covered in cartilage which lowers the friction between the two pieces of bone and dampens the forces. There is also a piece of cartilage called the labrum, surrounding the brim of the acetabulum. It deepens the socket and makes it more stable [10].

2.1.1 Anatomical terminology

Anatomical terms can be used to describe parts of the body in relation to each other, as shown in figure 2.2. Terms that are commonly used in this thesis are [11]:

- **Distal and Proximal**: Used to describe how close or how far something is from the origin in the torso. Proximal is closer to the torso and distal is further away.

- **Lateral and Medial**: Describes how close something is to the midline of the body. Medial is closer to the midline and lateral is further away.
- **Anterior and Posterior**: Used to describe how close something is to the front or back of the body. Anterior is closer to the front of the body and posterior towards the back.
- **Superior and Inferior**: Describes how close something is to the top of the head. Superior is closer to the head and inferior is further away.

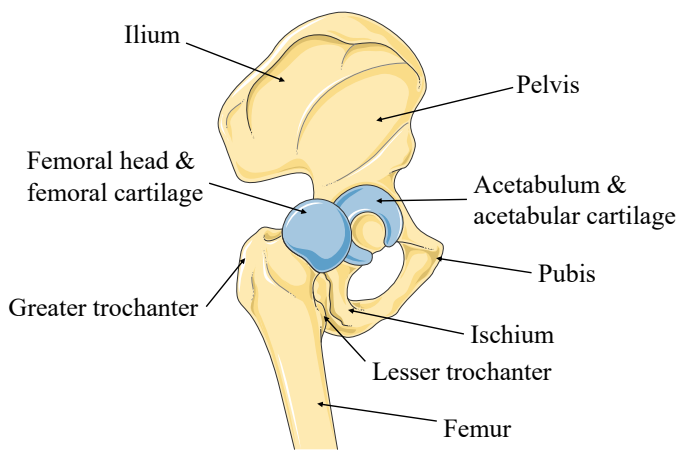

Figure 2.1: Illustration and description of the hip joint including femur, pelvis, and cartilage. Adapted from [12].

Anatomical planes can be used to divide the body into different sections. The three anatomical planes are, seen from the front as a person is standing up [11]:

- **Sagittal plane**: Divides the body into a right and left side and is a vertical plane.
- **Coronal plane**: Also a vertical plane, but divides the body into anterior and posterior.
- **Transverse plane**: A horizontal plane that divides the body into an upper and a lower part.

Anatomical terms can also be used to describe how parts of the body are moving relative to each other [13]. The movements in the hip joint are [9]:

- **Flexion and Extension**: Describes the change of angle of one part relative to another. Flexion occurs when the angle decreases and extension when it increases.
- **Medial rotation and Lateral rotation**: Describes rotation in relation to the midline. Medial rotation is towards the midline and lateral rotation is away.
- **Adduction and Abduction**: Describes movement relative to the midline. Abduction is a movement away from the midline and adduction is towards it.

.

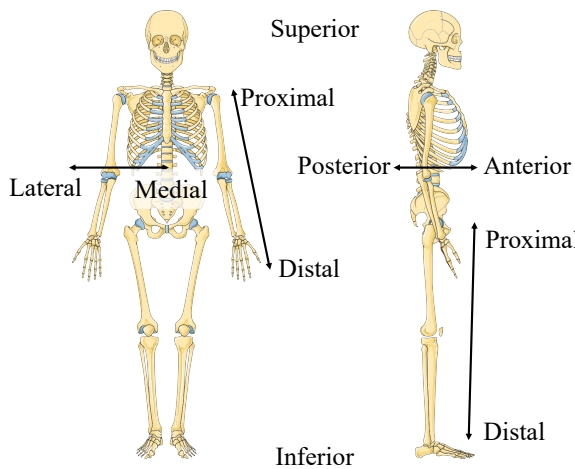

Figure 2.2: Anatomical directions shown on the human body. Adapted from [12].

2.1.2 Anatomy of the hip joint

Bone

Bone is a biological hard tissue that supports movements and protects some organs [14]. It is built up of collagen, water, hydroxyapatite minerals, proteoglycans, and noncollagenous proteins [15]. Bone can be divided into two types: cortical bone and trabecular bone. Cortical bone is denser and can be found on the surface of the bone as a thin shell or in the shaft of long bones. Trabecular bone is less dense, has a higher porosity, and can be found in the ends of long bones and in the vertebrae [14].

The mechanical behavior varies between the two types of bone, but has some similarities. Both cortical and trabecular bone have anisotropic behavior, which means it varies in different directions. The strength is greater in the longitudinal direction compared to the circumferential direction, and they are stronger in compression than in tension. For cortical bone, the stress-strain curve when loaded in the longitudinal direction can be approximated to be bilinear. It has a linear elastic region that ends with a distinct yield point before the linear hardening starts. For trabecular bone, the stress-strain curve does not have a clear linear region [14].

The bones in the hip joint are the femur and the ones making up the pelvis [16]. The femur is the longest bone in the body and its main function is to be weight-bearing and contribute to stability in the gait. The most proximal part of the femur, the femoral head, is connected to the acetabulum [17], a socket in the lateral part of the pelvis [16]. Close to the femoral head are two bony parts where muscles are attached, the greater trochanter and the lesser trochanter [17]. The pelvis consists of the two hip bones and the sacrum that joins them together. The hip bones consist of three parts each: the ischium, the ilium, and the pubis. The ilium is located in the superior part, the ischium in the inferior posterior part, and the pubis in the inferior anterior part [16].

A commonly used material model for bone in biomechanics is isotropic elastic materials [18, 19, 20] This is a simplification of the behavior of bone. An isotropic elastic material behaves the same in all directions and the stress is proportional to the strain. It can be described by Young's modulus (E) and Poisson's ratio (ν) [21]. The material parameters used in this thesis will be defined in chapter 3.4.3.

Cartilage

Cartilage is a soft tissue that mostly consists of water, collagen, and large proteoglycans [22]. There are several types of cartilage in the body with different functions. The type of cartilage found in the hip joint is called articular cartilage and cover the ends of bone [23]. The cartilage in the hip joint is made up of two parts, one that covers the femoral head and one that covers the acetabulum [24]. Its purpose is to provide a smooth surface and to be able to transfer loads with low friction. The thickness of the articular cartilage is 2-4 mm [23] and it decreases with age, beginning as early as school-age [25].

The structure and properties of cartilage, and the orientation of

the collagen fibers is depth-dependent (see figure 2.3). In the superficial zone, the collagen fibers are oriented parallel to the surface and make up 10-20% of the articular cartilage. In the middle zone, 40-60%, they are oriented in random directions. In the deep zone, 30% of the cartilage, the collagen fibers are perpendicular to the surface [22] and resists most of the compressive forces [23]. The amount of proteoglycans also varies with depth [22]. Below the deep zone, there is a thin layer called the calcified layer, which is attaching the cartilage to the underlying bone [23].

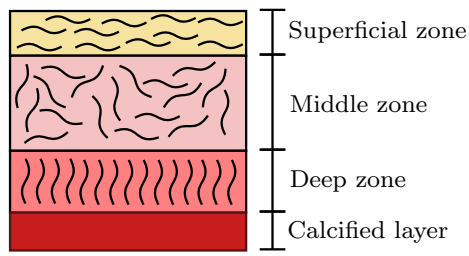

Figure 2.3: Cartilage is divided into zones, based on the orientation of the collagen fibers and the local composition of the tissue.

The mechanical behavior of cartilage can be described as being both non-linear and time-dependent [22]. It can be seen as a biphasic medium that has a solid phase and a fluid phase. When a force is applied, the interstitial fluid pressure increases, which causes the fluid in the cartilage to flow out. When the force is removed and the pressure is decreasing, the fluid moves back again. As the force is applied, the articular cartilage is stiffened which changes its mechanical properties. This produces a challenge in only having one set of material parameters for the articular cartilage [23], and to use a material model to describe all of its properties. Which material model is most suitable to use depends on the situation, but it is often beneficial to choose the simplest model possible that is still able to provide answers to the research question asked [22].

A simple material model for cartilage that is commonly used is a neo-Hookean hyperelastic material. This material model does not take into account all behaviors of cartilage, however, it has previously been used for cartilage in several FE models of the hip joint [18, 19, 20, 26, 27, 28]. It is a simple material model that has been shown to agree well with experimental studies [26]. A hyperelastic material has a non-linear response for larger strains and an elastic behavior for smaller strains. A

neo-Hookean hyperelastic material is based on the shear modulus (G) and bulk modulus (K) of the material [21]. A neo-Hookean hyperelastic material is described by equation 2.1, where C_{10} is half the bulk modulus and D_1 is twice the shear modulus. U is the strain energy per unit of reference volume, $\overline{I}_1$ is the first deviatoric strain invariant, and J^{el} is the elastic volume ratio [29]. The material parameters used for cartilage will be defined in chapter 3.4.3.

$$U = C_{10}(\overline{I}_1 - 3) + \frac{1}{D_1}(J^{el} - 1)^2 \tag{2.1}$$

Ligament

Ligaments attach bones to each other to maintain the correct position. They also restrict the relative movement between bones and are strong in resisting tensile loads. Ligaments consist of dense fibrous connective tissue that is built up by collagen, elastin and proteoglycans [15].

There are three major ligaments that form the hip joint capsule and attach the femur to the pelvis [24]:

- **Iliofemoral ligament**: The strongest ligament in the body. It limits extension and external rotation. It is attaching the anterior inferior iliac spine to the intertrochanteric line of the femur.
- **Ischiofemoral ligament**: Connects the posterior surface of the acetabular rim to the anterior aspect of the femur and limits internal rotation and adduction of the hip.
- **Pubofemoral ligament**: Attached to the anterior surface of the intertrochanteric fossa of the femur and the anterior part of the pubic ramus of the pelvis. This ligament limits the abduction and extension of the hip.

2.2 Biomechanics of the hip joint

The hip joint is crucial for walking and the ability a person has to walk depends on the anatomy and biomechanics of the hip. During gait and other movements, several forces are acting on the hip. When the hip is in motion, the conditions of static equilibrium are not fulfilled as the muscles surrounding the joint are generating forces. The acceleration of the moving parts during gait is relatively small compared to the forces from the muscles and the impact of gravity. One way of modeling gait

can therefore be by having the subject stand on one leg. A free body diagram of the hip joint can be seen in figure 2.4. The force R is the reaction force in the acetabulum, A is the force produced by the abductor muscle, and B is the weight of the body without the standing leg [15].

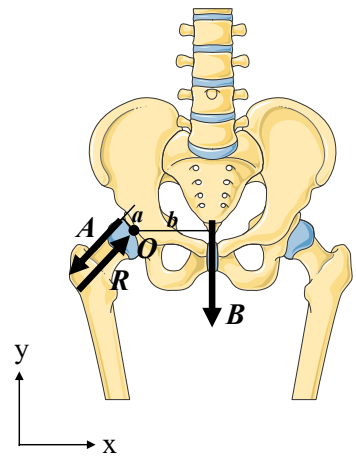

Figure 2.4: Free body diagram of a person standing on one leg, where the left leg of the subject is not touching the ground. R is the joint reaction force, A is the abductor muscle force and B is the weight of the body minus the standing leg. O is the center point for the movement, and a and b are moment arms. Adapted from [12].

Each of the lower extremities weighs approximately $\frac{1}{6}$ of the total body weight, which makes $B \approx \frac{5}{6}W$ where W is the entire body weight. With the center of the movement in point O, the moment in the joint can be described as in equation 2.2. The force in the acetabulum (A) is defined by equation 2.3. a and b are moment arms from the point O to the point where the forces A and B are acting [15].

$$\Sigma M = aA - bB = 0 \tag{2.2}$$

$$A = \frac{b}{a}B = \frac{5b}{6a}W \tag{2.3}$$

The forces acting on the joint are in equilibrium when standing on one leg. Assuming that the x-direction is horizontal and the y-direction is vertical, the total forces of the joint in the two directions can be calculated as in equations 2.4 and 2.5 [15].

$$\Sigma F_x = R_x - A_x = 0 \tag{2.4}$$

$$\Sigma F_y = R_y - A_y - B = 0 \tag{2.5}$$

2.3 Hip pathology

There are several hip deformities that can affect children. Some of the most common hip deformities can lead to OA if not detected early and treated properly [5, 30, 31, 32].

2.3.1 Osteoarthritis

Osteoarthritis is a degenerative disease where the articular cartilage wears down over time. OA is most common in the hands, knees, hips, and spine, but can affect any joint in the body. When the cartilage starts wearing down, the person will experience pain, stiffness, tenderness, and loss of flexibility. Bone spurs can form which are small pieces of protruding bone along the cartilage. OA can also cause inflammation in the joint and the surrounding tissue [1]. X-ray radiography is the most commonly used technique for OA diagnosis. The condition can be identified by the reduction of space between the acetabulum and the femoral head or by the presence of bone spurs [33].

2.3.2 Pediatric hip deformities

One hip deformity that can occur during childhood is Developmental dysplasia of the hip (DDH). DDH is an umbrella term for several anatomical differences in the acetabulum and the femoral head. A common representation of DDH is that the acetabulum is shallow or oriented in an abnormal direction. It can cause dislocation of the hip, and if left untreated, can lead to pain and OA during early adult years. Improving the development of the hip and preventing these problems in adulthood is therefore very important. The main risk factors for DDH are breech positioning in utero, being firstborn, female sex, and family history [5].

Femoroacetabular impingement (FAI) is a form of hip deformity that can occur as a child is growing. The basis of the condition is that extra bone will form on either of the two bones making up the joint. This will create an abnormal and irregular shape which can cause pain and

stiffness in the joint. If not detected, the misshapen bones will rub together unnaturally and may cause damage to the cartilage and labrum [30].

Another disease that can affect the hips of children is Legg-Calve-Perthes disease (LCPD). It occurs as the blood supply to the femoral head is temporarily interrupted. This causes the tissue in the bone to die and become necrotic. It will cause the bone to break apart and the femoral head may lose its rounded shape. The interruption of the blood flow will eventually be restored and the bone will start to regenerate. If the femoral head was already misshaped, this can cause problems to the joint and cause the child to limp, have pain, and become stiff in the joint. LCPD is most common in boys aged 4-10 [31].

One abnormality that can affect adolescents is Slipped capital femoral epiphysis (SCFE) and it is one of the most common hip disorders in the age group. The head of the femur will slip backward at the growth plate on the femoral neck. SCFE is more likely to appear in overweight adolescents or in association with a growth surge. Different endocrine disorders can also lead to an increased risk of developing SCFE. The disease has symptoms such as limping and pain in the groin, knee, thigh, or hip [32].

2.4 Medical imaging of the hip

DXA images, radiography images, and CT images were used in this thesis. They are three types of medical images commonly used to depict the hip. All techniques are using X-rays, but what images they produce and the risk they entail are slightly different [7].

2.4.1 2D X-ray images

X-rays are electromagnetic radiation of higher energy than visual light, which allows them to easily penetrate soft tissues. The amount of X-rays absorbed in different types of tissue, dependent on their composition and density, will create an image on a detector on the opposite side of the body. This 2D image is referred to as radiography [34]. Two standard projections can be produced when performing a radiography of a hip, anteroposterior view and lateral view [35].

DXA is a method that is used to measure bone density. It is primarily used for osteoporosis diagnosis and screening [36]. DXA uses X-rays

of two different energies as they are absorbed in different amounts in tissues of different densities. Based on this, an estimation of the density in bone and other tissues can be given [37].

2.4.2 X-ray Computed Tomography

CT is a medical imaging technique that produces 3D images of the subject, who is laying on a bed that moves during the scan. The X-ray source and detectors are rotating around the patient to scan from different angles. The scans are used to recreate a number of slices, using a mathematical process. The thickness of the slices can vary depending on the scanner used or be selected depending on what part of the body is examined. The scanning process is repeated until the whole region of interest is scanned. By adding all reconstructed slices together, it is possible to recreate a 3D image [7].

CT images are especially useful to image bones. The dense structure of the bone absorbs most of the X-rays and it is therefore easy to distinguish. It is also possible to examine other tissues using CT, but depending on their ability to absorb the X-rays, it can be difficult to separate them from each other. Contrast agents can be used to enhance soft tissue contrast by increasing X-ray absorption in specific locations [7].

The advantage of using CT compared to conventional X-ray radiography is that it produces a 3D image that contains more detailed information. However, there are some risks to using CT as the amount of ionizing radiation reaching the patient is much higher in comparison to conventional 2D X-ray imaging [7].

2.4.3 Radiation risks

All medical imaging that involves X-rays entails some risks to the patient. X-rays are ionizing radiation [7], that is, they have the ability to free electrons from atoms due to their high energy. In living organisms, this can lead to cell damage [38], and increase the risk of cancer [7].

Children are more sensitive to ionizing radiation compared to adults and it is therefore especially important to be careful when exposing them to ionizing radiation. They are also expected to live longer after exposure and it is important to give low doses to children to reduce the risk of developing cancer in the future [7].

2.5 Machine learning

Machine Learning is a branch of artificial intelligence where algorithms can be trained on sets of data to predict the result of new, unseen data and thereby create new original answers. ML algorithms can be either unsupervised or supervised [39].

Unsupervised ML has no known answers to the data, also known as ground truth. Instead, it has to find patterns in the images to base the prediction on. Unsupervised ML can for example be used for denoising data or data comprehension. Sometimes, unsupervised ML can be used before supervised ML to gain a better understanding of the data [39].

Supervised ML is more common in the field of object detection and uses annotations to train the algorithm for their prediction. It can be used for example to perform classification, regression, object detection, and segmentation. Successful training of a supervised ML algorithm requires input data, corresponding outputs, and a method to determine the algorithms performance [39]. In this thesis, two methods for supervised learning have been used.

When using an ML algorithm, it will be trained, validated, and tested. This is done by using different sets of the data, train, test, and validation [40]. The training set is a portion of the actual data that the algorithm sees and uses to learn what is of interest in the data. The validation set is sometimes separated from the test set and is used to fine-tune the ML algorithm. The validation set can see the original data but does not learn from it. The test set is only used when the ML algorithm is trained and is used to evaluate the accuracy of the predictions [41].

2.5.1 Automatic landmark detection

A landmark is a point in an image that is of specific interest that contains useful information and is stable when the image changes. Landmarks can be divided into three categories [42]:

- **Anatomical landmarks**: Points in a morphological image that are of interest due to the biological meaning of the position. They will have the same position in images of different (healthy) specimens.
- **Mathematical landmarks**: Landmarks placed based on mathematical properties of a feature in an image such as a curve or

angle.

- **Pseudo-landmarks**: Constructed points located between anatomical or mathematical landmarks, for instance, used to create more sample points.

The type of landmarks used to annotate the images in this thesis is anatomical landmarks.

2.5.2 ML-moprh for landmark detection

One case where ML has been used to automatically detect landmarks in morphological images is presented in *ML-morph: A fast, accurate and general approach for automated detection and landmarking of biological structures in images* by Porto and Voje [40]. This manuscript describes the development of a supervised ML algorithm for automatic prediction of landmark placement. Its capabilities are illustrated through the detection of biological structures in Drosophila wings, sea bass, and a bryozoan colony.

ML-morph depends on a set of parameters to be tuned for optimal performance in a specific application. ML-morph is divided into two parts: object detection and shape recognition. Object detection is performed to detect the position of the object of interest in the image. This is done based on the manual annotations and thereby, the algorithm will identify the object location in the image. ML-morph uses a histogram of oriented gradients (HOG) to describe the image. Image regions are randomly extracted in each training image using bounding box annotation. The HOG features of the box are then extracted and a new set of images is created. A structural support vector machine is then trained on the new set of images to classify an image based on whether a region is positive, contains the object, or negative, does not contain the object. To detect the object, a sliding window is passed over the image and in each position, based on a threshold value, determines if the window contains an object. ML-morph then performs 10-fold cross-validation on the object detector to prevent overfitting errors [40]. In the object detection part of the algorithm, several parameters are possible to change to fit the algorithm to the data:

- $\boldsymbol{\epsilon}$: Epsilon, ϵ, is the insensitivity parameter. It corresponds to a zone where there is no penalty assigned to errors. This means that a high value of ϵ will allow larger errors [40].

- **C parameter**: The C parameter will determine the distance between the hyperplane that separates the two classes (object and not object) and the closest data point. This can also be referred to as the size of the margin [40].
- **Upsample limit**: To upsample the data means that artificially generated data points are created from the minority class, the type of data with least occurrences, to balance the class label. Upsampling can be done in several different ways such as duplicating existing points or using algorithms such as K-nearest-neighbors [43].
- **Window size**: The sliding window will pass over the image and whenever the image passes a threshold test, the output is that there is an object. This is expressed as the height multiplied by the width of the window [40]. The window must be large enough to be able to detect the changes in intensities in the image but small enough not to miss small details [44].

The next step of the ML-morph algorithm is shape detection. Object-specific automated landmark detection is performed by a cascade regression algorithm. Iteratively, the cascade regression will find the shape of the object from the sparse subset of pixel intensities in the image. If object detection is used, only the area of the image where the object is located will be used for cascade regression [40]. The shape detection part of the algorithm also has several parameters that can be modified:

- **Tree depth**: The depth of the regression tree used in the method [40]. A regression tree is a type of decision tree that can be used to make quantitative predictions. A decision tree will recursively make decisions at splitting nodes to eventually end at a singular point where only one option is possible [45].
- **Cascade depth**: The cascade depth is the number of times the shape is updated based on the local pixel patterns during the prediction. The depth is hence the number of increments between the initial 'guess' of the shape and the final predicted shape [40].
- $\boldsymbol{\mu}$: μ is a regularization parameter. Regularization means that the algorithm will have a preference for one solution over the other when deciding between two equal [46].
- **Oversampling**: Oversampling reduces the impact of an imbalanced datasets. This is done by generating synthetic samples of the minority class to make the number of data points for each class more balanced [47].

The number of threads can be altered in both the object detection and the shape detection to increase or decrease the time ML-morph takes to run [40]. Using threads, several processes can be executed simultaneously and independently of each other, which allows some processes to keep running even if another is performing an operation that takes a long time [48].

There are two versions of the ML-morph available, 'original ML-morph', oML-morph, and 'simple ML-morph', sML-morph [49]. The difference between the oML-morph and the sML-morph is that the simple version assumes that there is only one object in the image and therefore it does not do object detection, only shape detection. Both the sML-morph and oML-morph were evaluated in this thesis.

2.5.3 Other ML algorithms for landmark detection

Another example of an algorithm where ML is used to automatically detect landmarks, is the implementation of convolutional neural networks (CNN) by Le et al., to detect anatomical landmarks in images of a beetle [50]. CNNs have several layers that predict the outcome based on the output of the last layer. Common types of layers are convolutional, pooling, dropout, and full-connected layers [50]. Another example is a manuscript by Mehryar et al. where 3D images of human faces are used in automatic landmark detection. The algorithm in question uses curvature-based landmark detection where the surface of a face is used to find regions of interest by using Gaussian and mean curvatures [51]. In a third manuscript by Manacorda et al. Procrustes analysis was used to perform shape analysis and landmark prediction in images of plants. In this case, the specimens had a much larger deviation in appearance, and therefore, performing shape analysis to out rule information that is not relevant is highly beneficial [52].

ML-morph was used in this thesis as it is a complete algorithm, ready to use, and developed to detect anatomical landmarks in morphological images. It was also easy to adapt ML-morph to the data used in this thesis.

2.6 Subject-specific FE modeling

The finite element method is a numerical method to obtain approximate solutions for partial differential equations. It can be used for one-, two-,

or three-dimensional regions. The basis for all calculations is that the whole geometry is divided into small pieces, finite elements, for which the calculations are made. By dividing the region into smaller elements, it is possible to find an approximate solution for each element instead of the entire region. By then adding the solution for all elements together, it is possible to find a solution for the whole region. All the elements form a FE mesh [53].

Finite element analysis (FEA) is a useful tool in biomechanics. It can be used to model the response of the hip during various activities to evaluate how the cartilage in the hip is affected [26].

The starting point of solving a FE formulation of a problem is known as the strong form and it describes the physical system to be solved. From the strong form, the weak form is obtained. The strong form is multiplied by a weight function chosen following the Galerkin method and integrated over the elements. In a simple one-dimensional mechanical problem, this results in equation 2.6 [53].

$$\left(\int_a^b \mathbf{B}^T AE\mathbf{B}dx\right)\mathbf{a} = -[\mathbf{N}^T A\epsilon]_a^b + \int_a^b \mathbf{N}^T bdx \tag{2.6}$$

$\mathbf{B} = \frac{d\mathbf{N}}{dx}$, A is the cross-sectional area, E is Young's modulus, $\mathbf{a}$ is the nodal displacement, $\mathbf{N}$ is the shape function, ϵ is the strain, and b is the forces acting on the body. From equation 2.6 the standard FE formulation in mechanical problems is obtained:

$$\mathbf{Ka} = \mathbf{f} \tag{2.7}$$

$\mathbf{K}$ is the stiffness matrix and is equal to $\mathbf{K} = \int_a^b \mathbf{B}^T AE\mathbf{B}dx$. $\mathbf{f}$ is the force vector that is obtained by adding the boundary vector ($\mathbf{f_b} = -[\mathbf{N}^T A\epsilon]_a^b$) and load vector ($\mathbf{f_l} = \int_a^b \mathbf{N}^T bdx$) together, and $\mathbf{a}$ is the displacement vector. By solving this equation for each element, and adding them together, a solution for the whole body is obtained [53].

In this thesis, Abaqus [54], a FEA software, is used to find the solution to the standard FE formulation and perform the analysis of the FE models of the hip joint.

2.6.1 Image Segmentation

In biomedical applications, the geometries of interest are often segmented from clinical images such as CT images or images from magnetic

resonance imaging (MRI). As tissues in the body have different densities, the image will have varying intensities and thus making tissues possible to distinguish from each other. The segmentation can be made either automatic or semi-automatic, depending on the type of tissue. Especially the cartilage in the hip can be difficult and time-consuming to segment since it consists of two parts, one on the femoral head and one on the acetabulum, and they are very close together. Contrast agents are often necessary to distinguish the cartilages in the hip joint when CT images are used. Due to the difficulties in segmenting cartilage, attempts have been made to approximate the geometry of the cartilage in different ways. This reduces the time it takes to perform the segmentation, but the results do not correspond completely to results from experimental studies [18].

In this thesis, CT images of the hip joint were used. The segmentation was performed using a semi-automatic approach.

2.6.2 Elements and mesh

A mesh consists of all finite elements needed to describe the geometry. Various types of elements and element sizes can be used to produce the mesh. Tetrahedral elements and hexahedral elements are two types of elements that are commonly used in 3D FE models (see figure 2.5). Tetrahedral elements can often be more easily generated for complex geometries, like biological structures. In softer tissues, there can be a problem with tetrahedral elements as they can be too stiff in large deformations, it is therefore often preferred to use hexahedral elements. To generate a hexahedral mesh is often more time-consuming compared to a tetrahedral mesh. The reason is that there are many robust alternatives for generating a tetrahedral mesh, and only some limited options for generating a hexahedral mesh [22]. In this thesis, both four-noded tetrahedral elements and eight-noded hexahedral elements were used.

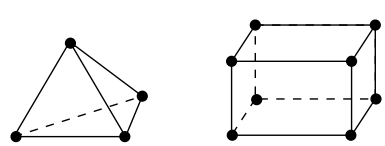

Figure 2.5: The left figure is a four-noded tetrahedral element and the right figure is an eight-noded hexahedral element.

Chapter 3

Materials & Methods

3.1 Material

In this thesis, 2D X-ray images and 3D X-ray CT images were used. The images used are presented below. The images are of adults as this thesis was a first attempt to develop the tool presented. It is also harder to access images of children.

3.1.1 2D X-ray images

One set of images used were manually annotated DXA images of the pelvis and femur. The images are from the MrOs Sweden study, captured in Malmö and Uppsala [55]. The images were collected in a study of adult males affected by osteoporosis. The subjects in the images were between 69 and 80 years old. The study included 2008 subjects and in this thesis, 2042 images of one of the hips were used, some of the right hip and some of the left, and mirrored to all face the same direction. As the images are of different sizes, each image had been padded to obtain a final image size of 295x212 pixels. Each pixel is 0.6 mm in the x-direction (lateral-medial) and 1.05 mm in the y-direction (inferior-superior). As the images were in jpg format, the pixels in the images were isometric. The manually annotated landmarks for each image were used as a ground truth. There are eight landmarks in each image, which are depicted in figure 3.1 and explained in table 3.1. The images were annotated prior to the start of this thesis project by Dr. Lorenzo Grassi as part of a separate, ongoing study.

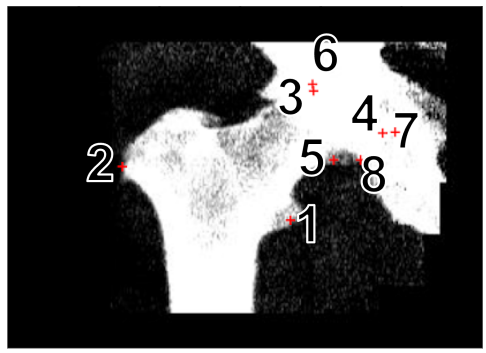

Figure 3.1: Manual annotations on a DXA image of the hip. 1: lesser trochanter, 2: greater trochanter, 3: on the superior side of the femoral head, 4: on the medial side of the femoral head, 5: on the inferior side of the femoral head, 6: on the superior side of the brim of the acetabulum, 7: on the medial side of the brim of the acetabulum, 8: on the acetabular labrum.

Table 3.1: Location of landmarks seen in image 3.1.

Landmark	Explanation
1	On the medial point of the lesser trochanter
2	On the most lateral part of the greater trochanter
3	On the superior side of the femoral head
4	On the medial side of the femoral head
5	On the inferior side of the femoral head
6	On the superior side of the brim of the acetabulum
7	On the medial side of the brim of the acetabulum
8	On the acetabular labrum

Another type of images that were used in the automatic landmark detection were radiography images. The dataset used is called *Pelvis-X-ray_Segmen-tation_Database* (see figure 3.2), and was accessed through GitHub, licensed under an MIT license [56]. The dataset was created at the Center for Artificial Intelligence at Chang Gung Memorial Hospital on the 5th of August 2020. Version 1.0.0 of the dataset was used. The images in the database are anteroposterior pelvis radiograph assessments of 400 subjects, captured at Chang Gung Memorial Hospital. 205 of the images were used in this thesis. The sizes of the images are $(1600 \sim 2700)$ x $(1600 \sim 2700)$ pixels.

Figure 3.2: A radiography image of the hip.

3.1.2 CT image

The CT image used for the subject-specific FE model came from a cadaveric hip joint from a multiscale data collection (see figure 3.3) [57]. The image is of an 81-year-old female who weighed 63 kg with no history of musculoskeletal disease. The image includes the whole lower body including the hip, leg, and foot. The size of each slice is 512x512 pixels and has an isotropic pixel size of 0.98 mm, and the image has a total of 1120 slices. No contrast agent was used, which means that the denser tissues such as bone were more prominent in the image while softer tissues such as cartilage were harder to distinguish [7].

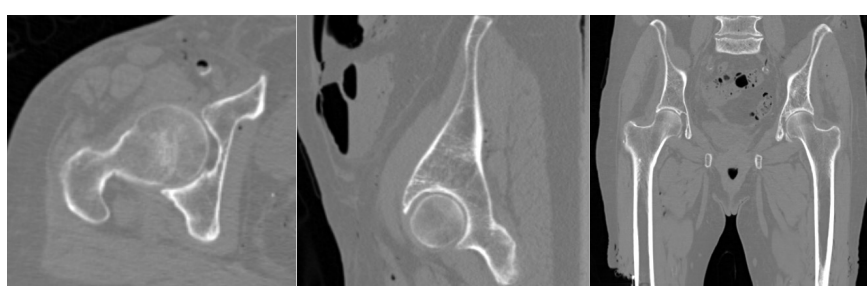

Figure 3.3: The CT image of the 81-year-old female used for the subject-specific FE model. Sagittal view (left), transverse view (middle), and coronal view (right).

3.2 Overview of the methods

The first part of the thesis was focused on image analysis and ML and the goal was to automatically detect landmarks in DXA images of the

hip. In the second part of the thesis, the goal was to develop a CT-based FE model of the hip cartilage contact. The two parts were then combined to create FE models of the hip based on automatically detected landmarks in DXA images.

3.3 Automatic landmark detection

This section of the thesis evaluated the possibility of using ML to automatically detect landmarks in DXA images of the hip joint. This has been done by using an algorithm by Porto and Voje [40, 49] and by researching the possibility to use other alternatives.

3.3.1 ML-morph

The output of the oML-morph that uses shape detection and object detection, and the sML-morph that uses only shape detection, is the coordinates of the predicted landmarks. Below, different ways ML-morph has been used and how the images have been augmented will be presented. An overview of the workflow of the automatic landmark detection can be seen in figure 3.4.

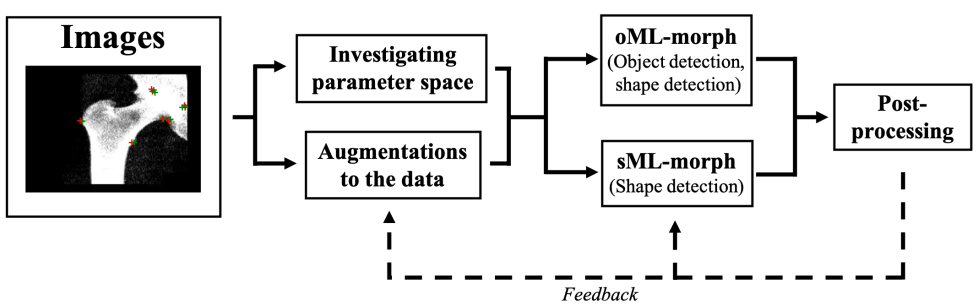

Figure 3.4: Overview of the automatic landmark detection using ML.

Testing different parameters

To make the oML-morph and sML-morph applicable to the DXA images used, several combinations of the parameters introduced in chapter 2.5.2 have been tested. Provided with the code for ML-morph was an example of parameter values used on the images of drosophilid wings. These parameters were initially used to test the ML-morph on the DXA images

and were in this thesis used as a guide when investigating the parameter space.

The parameter study was comprised of varying one parameter at a time. The parameter values used in this thesis can be seen in table 3.2. The parameters in oML-morph were evaluated first and started with the parameters used for object detection. The window size parameter was evaluated first as some values of the parameter would give errors and some images would be excluded. Therefore, a value of the window size that included all images was found, values above and below were tested and the best value found was kept for the rest of the testing of object detection. The number of threads, ϵ, and C were varied one at a time, in the same manner as the window size. The up-sample limit for the object detection was not investigated as the example from ML-morph did not. The parameters in the shape detection were then evaluated for oML-morph in the order seen in table 3.2, by increasing and decreasing the value of each parameter and picking the value that gave the most accurate predictions. The best parameter set was then used as a base and each value was varied again in the order of table 3.2. This was then done one more time for the new best set of parameters. In total, 85 different sets of parameters were tested for oML-morph.

Table 3.2: The parameters that was investigated as well as ranges tested.

	Parameter	**Tested values**
Object detection	Threads	1, 7, 10
Object detection	ϵ	0.001, 0.01, 0.1, 1
Object detection	C	1, 5, 10
Object detection	Window size $*10^3$	2, 3, 4, 4.1, 5, 5.5, 6, 10
Shape detection	Threads	1, 2, 4, 7, 10, 15
Shape detection	Tree depth	1, 2, 3
Shape detection	Cascade depth	1, 10, 20, 25, 30, 50
Shape detection	μ	0.001, 0.01, 0.02, 0.03, 0.04, 0.05, 0.06, 0.07, 0.08, 0.09, 0.1, 1
Shape detection	Oversampling	10, 25, 75, 100, 200, 500, 1000

All parameter sets for the shape detection used by oML-morph was tested on the sML-moprh as well. The best set of parameters using sML-morph was then used as a base and each of the parameters were changed slightly, one at a time, to find the set with highest accuracy.

In total, 87 different sets of parameters were tested for sML-morph.

When determining the best parameters, the same sets of images were used for training and testing. Out of all the images, 80%, 1664 images, were used for training and the other 20%, 408 images, were used for testing and validation. The performance of each test of the automatic landmark detection was evaluated in two ways: 1) the mean of the euclidean distance between each automatically detected landmark, and its corresponding manually annotated landmark for each image, *ME* (Mean Euclidean), 2) the mean of the maximum, minimum, and mean distance in the the distance in the x-direction (lateral-medial) and the y-direction (inferior-superior), and the euclidean distance for each image, *MA* (Mean All). *ME* was used to evaluate the mean performance of the automatic landmark detection and *MA* to include the presence of outliers. Euclidean distance was used by Porto and Voje as well to determine the efficiency of the shape detector [40].

Attempts to improve the accuracy

Several ways of pre-processing and augmenting the images were performed to see how the performance of the ML-based landmark annotation would be affected.

When running the oML-morph, a larger deviation in the x-direction (lateral-medial) was shown. To evaluate this, the DXA images were rotated 90° counterclockwise. The rotated images were tested with three different sets of parameters, twice each, giving a total of six runs. It was tested on both the oML-morph algorithm and the sML-morph.

Another attempt at improving the performance of the algorithm was to mask the images. This was performed to examine if the automatic landmark prediction would be more accurate if the contrast between different areas in the images was higher. This was done by creating a binary, 'masked' version of the DXA image where any pixel above 20% of the intensity in an image was gray and the other was black. The masked image was then tested on the sML-morph on a selection of different parameters. The next step of the masking process was to create a filled-in outline of the hip. This was done by a series of dilation and erosion. When using the dilation command, all holes in the image increased by one pixel in each direction. As the black background is considered a big hole by python, the specks in the background of the image were removed. The erosion command does the opposite of the dilation and increased the size of the holes, removing the specks in the

object in the image [58]. The outline of the femur was used as a template to create a 'double-masked' image where the intensities of the original image were saved in the bone regions but the noise in the background was removed. An example of producing the masked images can be seen in figure 3.5. This was tested on only the sML-morph on three different sets of parameters.

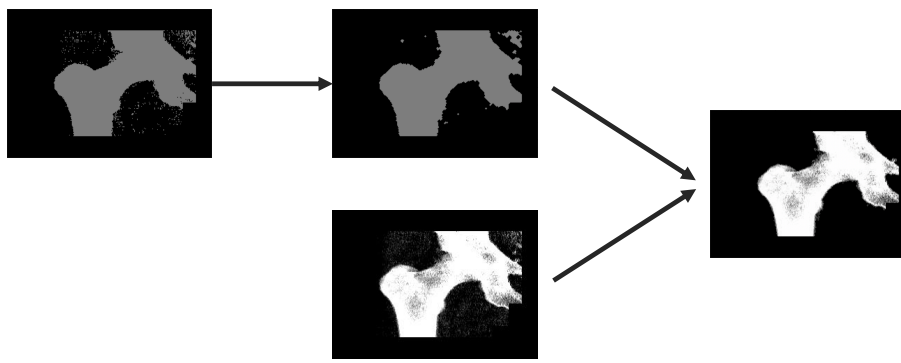

Figure 3.5: Overview of how the masked images were created. Left: masked image. Middle, top: binary image. Middle, bottom: original image. Right: double-masked.

Radiography images

The images from the Chang Gung Memorial Hospital dataset were interesting to use as they are radiography images. This will test the robustness of sML-morph as they were captured with another imaging method than the DXA images.

The images from the new dataset were tested and evaluated using the six best parameter sets from the DXA images and used with the sML-morph. The images in the radiography dataset were first split in half to only contain one hip each, and half of the splits were flipped to all face the same direction. Next, the radiography images were cropped and padded to make the proportions of the radiographs the same as the DXA images, though the size of the image would still be different. Predictions of the landmarks in the cropped images were then done by sML-morph, previously trained on only the DXA images. 205 of the cropped radiography images were annotated and sML-morph was trained and tested on the images. Using only the radiography images was done to test the robustness and to see how well hips in radiography

images would be predicted when trained on radiography images. Lastly, the 205 radiography images were mixed into the DXA images and sMLmorph was trained and tested.

3.4 CT-based FE model of the hip joint

The methodology for the subject-specific FE models of the hip joint was divided into three main parts: pre-processing, processing, and post-processing. The pre-processing included segmentation to create a 3D model of the geometry and generating a FE mesh of each part (pelvis, femur, and both cartilages). The workflow for meshing bone (pelvis and femur) and cartilage (acetabular and femoral cartilage) differed as described in more detail in each section. Processing included the simulation of the FE model, and post-processing was focused on analyzing and comprehending the results. An overview of the workflow can be seen in figure 3.6.

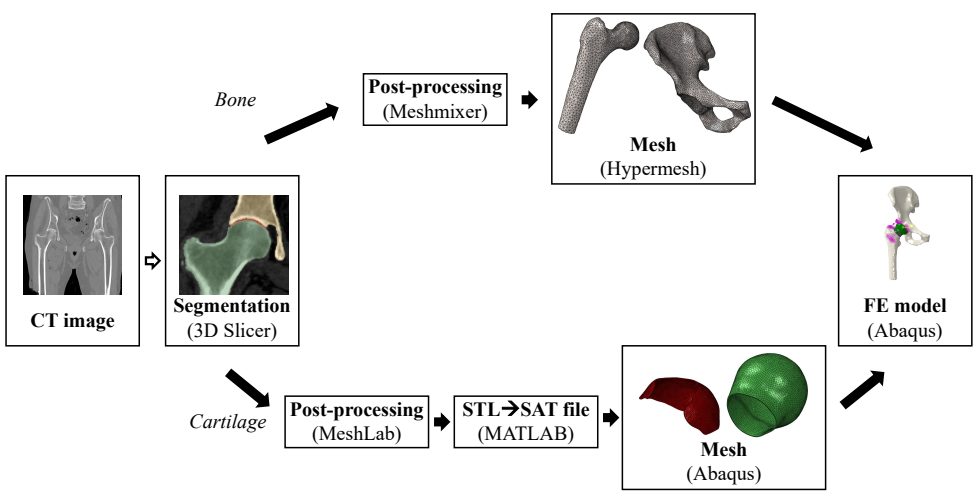

Figure 3.6: The workflow for creating the FE model from the CT image.

3.4.1 Segmentation

The CT image of the right hip joint was segmented using the software 3D Slicer [59]. The goal was to segment the proximal femur, pelvis, and

the gap between the bones as cartilage (see figure 3.7). The cartilage was segmented as a single part due to the difficulty in separating them from each other in the image. The goal was to later separate the cartilage into two parts: femoral cartilage and acetabular cartilage. The labrum was excluded as it does not provide a significant contribution to the load support in the hip joint [60, 61].

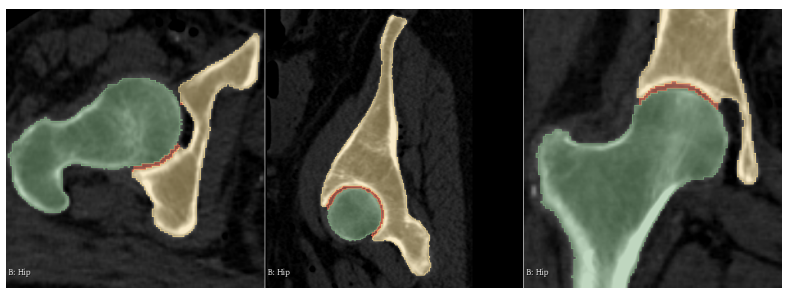

Figure 3.7: Segmentation in 3D Slicer. Coronal, sagittal, and transverse view. The green areas are the femur, yellow are the pelvis, and red are the entire cartilage.

The segmentation was performed using a semi-automatic approach. The pelvis and the proximal femur were mostly segmented using a threshold tool that marked all pixels within an intensity interval. However, manual segmentation was needed to segment the complete bones. When segmenting the bone, both types were considered cortical bone as modeling them separately has shown to have a small impact on cartilage contact mechanics in FE models of the hip joint [27, 62].

The contrast between cartilage and other soft tissues in the image was low, which made it difficult to use an automatic approach. Cartilage was mostly segmented by manually selecting all pixels in the gap between the segmented pelvis and femur, carefully avoiding any overlap. The thickness of the segmented cartilage was later decreased to be approximately half the thickness of the gap, to only correspond to the acetabular cartilage. The femoral cartilage was made in the post-processing of the surface mesh.

All parts that were segmented in 3D Slicer were exported separately as STL files including a surface mesh consisting of triangular elements.

Post-processing of the surface mesh

When doing post-processing of the segmented parts, Meshmixer [63] and MeshLab [64] were used for bone and cartilage, respectively. In both software, similar post-processing was performed. The main steps included reduction of the triangular surface mesh by increasing the element size and smoothing the surfaces to remove small irregularities. For the bones, the amount of reduction of the mesh varied between different parts of the geometry. In the areas that were in contact with cartilage, the size of the elements was smaller than in parts that were not in contact. The reason for that was to have an element size closer to the one used for cartilage. The reduced and smoothed mesh for all parts were exported as STL files.

To make the part representing the femoral cartilage, Meshmixer was used. The segmented femur was cropped to only include the part of the femoral head that is covered in cartilage. An offset of 1 mm from the surface (approximately half the thickness of cartilage in a healthy subject) was made to represent the femoral cartilage. Post-processing, which included smoothing and reduction of the triangular surface mesh, was performed in MeshLab.

3.4.2 Generating the mesh

Cartilage was modeled using hexahedral elements and bone using tetrahedral elements, which resulted in different pipelines for FE mesh generation. Tetrahedral elements are beneficial for more complex geometries and hexahedral elements are preferred to use for softer tissues like cartilage, as mentioned in chapter 2.6.2. These types of elements have been used previous to this thesis, modeling both bone and cartilage in several FE models of the hip joint [18, 19, 20, 26, 62, 65]. Generating the mesh for bone had a more automatic approach while generating the mesh for cartilage required more manual work.

Bone

The mesh for the pelvis and femur was generated using HyperMesh [66] (see figure 3.8). The element size in the tetrahedral mesh was based on the size of the triangular elements in the surface mesh. The mesh for both pelvis and femur was exported as Abaqus input files. The meshes of the femur and pelvis had 86,451 and 129,400 tetrahedral elements.

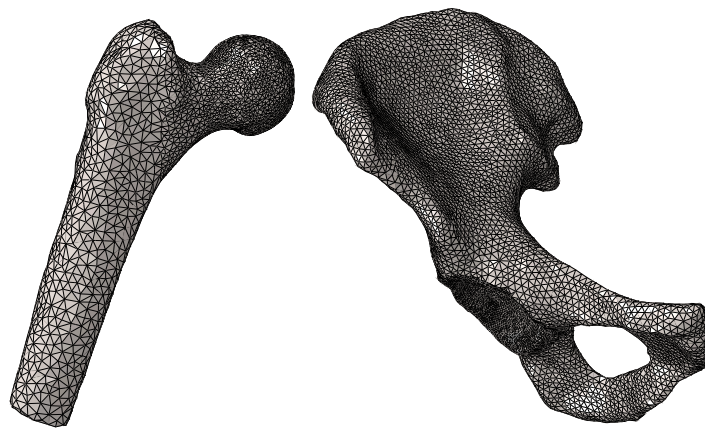

(a) Femur **(b)** Pelvis

Figure 3.8: The tetrahedral meshes used for the femur and the pelvis.

Cartilage

An initial attempt was made to generate the mesh for cartilage in HyperMesh. Due to the complex geometry of cartilage, and that hexahedral elements were used, it was more complicated to generate the mesh in HyperMesh compared to the mesh for bone. Two methods for generating a hexahedral mesh in HyperMesh were explored, they either changed the geometry or resulted in a highly unstructured mesh. Other options were explored and resulted in a mesh generated using Abaqus.

When generating the hexahedral mesh, a guide by Paul Bolcos in Simuleon FEA Blog was followed [67]. To generate the mesh in Abaqus, the STL file including the triangular surface mesh from MeshLab, had to be converted into an SAT file. The conversions were performed using MATLAB code for an STL to SAT converter by Adam H. Aitkenhead [68]. The SAT files were then imported as parts into Abaqus, one part representing the acetabular cartilage and one part representing the femoral cartilage. A small portion of the edges of each cartilage was manually cut off, by marking and removing the edges after manual inspection, to receive straight edges. By cutting off the edges, the most uneven parts of the cartilages that made it difficult to generate a mesh, were removed. Since only a small portion of the edge was cut off, the effect this simplification had on the model is minimal [67]. For both cartilages, the mesh was generated using the sweep mesh technique in Abaqus.

The acetabular cartilage, that had the entire segmented cartilage as a starting point, had to be reduced in thickness to only correspond to half the gap between the bones. The mesh was created for the whole segmented cartilage and later decreased in thickness. Both the element size and the number of elements through the thickness were specified before the mesh was generated. The element size used for the acetabular cartilage was 0.7 mm. Initially, the thickness of the mesh was ten elements, increasingly smaller in thickness towards the center of the mesh. The seven layers of elements closest to the femoral head were then removed to only keep a thin slice of the mesh as the acetabular cartilage. The thickness of the final acetabular cartilage was thus three elements and varied in different parts in a range of 0.45-0.83 mm. The thickness in mm of the final acetabular cartilage was later adjusted to fill the gap between the femoral cartilage and the acetabulum. The mesh used for the acetabular cartilage is shown in figure 3.9 and had a total of 70,201 elements.

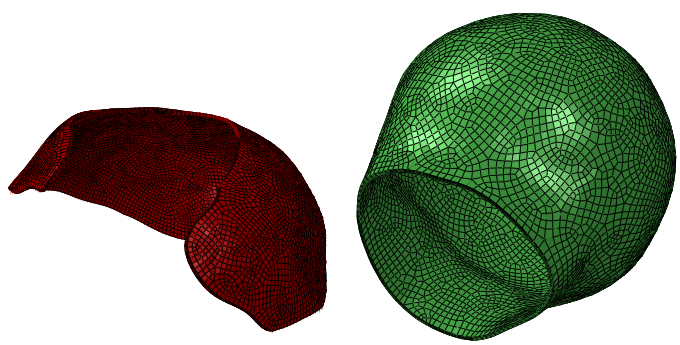

(a) Acetabular cartilage **(b)** Femoral cartilage

Figure 3.9: The hexahedral meshes used for the acetabular cartilage and the femoral cartilage.

The mesh for the femoral cartilage was generated in the same manner as the acetabular cartilage and had a total of 18,606 elements. The element size used was 1 mm. Since the offset from the femoral head used to make the femoral cartilage was slightly larger than half the average distance between the femoral head and acetabulum, the thickness of the femoral cartilage was also decreased by removing layers of elements. The initial mesh was five elements thick, with the smallest elements in the center of the mesh. The two layers of elements closest to the acetabulum were removed which resulted in a mesh of the femoral cartilage that was

three elements thick (see figure 3.9). The final thickness of the femoral cartilage was approximately 0.6 mm which was approximately half the thickness of the gap between the femoral head and the acetabulum.

3.4.3 FE model

Several FE models of the hip joint were developed using Abaqus/CAE 2020 [54]. The models can be divided into two groups, one that modeled standing positions and one that modeled gait. A few options for material parameters, constraints, and boundary conditions were used and compared. The results from the different FE models of the hip were also compared to the literature [20, 26, 27, 28, 65].

Material models and material parameters

In this thesis, bone was modeled as an isotropic elastic material. It is a material model that is commonly used in FE models of the hip joint [18, 19, 20]. The material parameters used for bone were the same in all the models made in this thesis, and the parameters used were $E = 17$ GPa and $\nu = 0.29$ [18, 19, 20, 26, 27].

As mentioned in chapter 2.1.2, cartilage has a complex behavior and that makes it challenging to find a material model that includes all its properties. In this thesis, cartilage was represented as a neo-Hookean hyperelastic material. By using a hyperelastic material model, the nonlinear stress-strain relationship of cartilage were included in the models [69]. One part of the thesis was to evaluate different sets of material parameters for cartilage to find what agreed the best with experimental studies and previous FE models of the hip. This was done by testing four sets of material parameters [20, 26, 28], as can be seen in table 3.3. C_{10} and D_1 are two parameters related to the shear modulus and bulk modulus, as described in chapter 2.1.2, and were used in Abaqus to describe the neo-Hookean hyperelastic material.

Table 3.3: Material parameters used for cartilage.

	$\mathbf{C_{10}}$ **[MPa]**	$\mathbf{D_1}$ **[MPa^{-1}]**
Cartilage A [28]	2.043	0.051
Cartilage B [26]	3.4	0.029
Cartilage C [26]	3.4	0.003
Cartilage D [20]	6.8	0.0015

Interactions and constraints

Interactions and constraints in Abaqus were used to define how the different parts of the models interacted with each other and were connected. A few different types of constraints were used for the FE models [29]:

- **Rigid body constraint**: The movement of the region was constrained to a reference point. This means that the relative position for the whole region was constant and there was no deformation in the elements.
- **Tie constraint**: Made it possible to combine parts by tying the surface nodes together.
- **Coupling**: Allowed to control the motion of a surface using a reference point.

Either tie constraints or rigid body constraints were used between the femur and femoral cartilage as well as the acetabulum and acetabular cartilage. When tie constraints were used, coupling was also used for the femur to connect the surface to a reference point in the center of the femoral head. Tie constraints were used to model deformable bones and rigid body constraints were used to model rigid bones.

In addition, a contact interaction, surface-to-surface, was used, which was applied between the two cartilages. One surface was defined on the femoral cartilage, the 'master surface', and one was defined on the surface of the acetabular cartilage, the 'slave surface'. The surface-to-surface interaction was defined as a hard contact with frictionless sliding. In the surface-to-surface interaction, the two surfaces were adjusted to fill the gap between the cartilages without overlaps. The nodes on the surface of the acetabular cartilage were moved to the surface of the femoral cartilage.

Hip joint coordinate system

The global coordinate system of the hip model was used for the pelvis and acetabular cartilage. The x-axis was defined in the lateral-medial direction, the y-axis in the inferior-superior direction, and the z-axis in the anterior-posterior direction.

The local coordinate system for the femur was found by using four coordinates in the femur, found by using a MATLAB function by Fischer et al. [70]. To use the MATLAB function, the whole femur was needed. Since only the proximal part of the femur was segmented, the previous

segmentation was extended to include the complete bone. The segmentation, post-processing, and generation of the mesh were performed as previously described. The whole femur was only used to define the center of the femoral head and to find the femoral coordinate system. In the FE models, only the proximal part of the femur was used.

From the MATLAB function by Fischer et al., the coordinates of the four points in the femur were obtained. In addition to a point in the center of the femoral head, three other points were used to define the local coordinate system for the femur. The local coordinate system was defined by following the recommendation for the hip joint coordinate system from the International Society of Biomechanics (ISB) [71], and using the coordinate of the points of interest from the MATLAB function. This resulted in an x-axis of the local coordinate system for the femur that was parallel to the one in the global coordinate system, using the point in the center of the femoral head, and another point on the x-axis of the global coordinate system. The y-axis of the femoral coordinate system was defined using two points on the femur, one on the intercondylar notch and one in the middle of the shaft. The third axis, the z-axis, was defined to be perpendicular to the x- and y-axis of the femoral coordinate system.

One leg standing

The first loading scenario to be modeled was one leg standing. Five different models were developed and compared, which included different material parameters and constraints. All four sets of material parameters for cartilage were used, and cartilage A was used in two models, one using rigid body constraints and one using tie constraints. All models of one leg standing can be seen in table 3.4.

Table 3.4: A summary of all models that simulated one leg standing.

	Cartilage	**Constraint**
Model 1A	A ($C_{10} = 2.043$ MPa, $D_1 = 0.051$ MPa^{-1})	Rigid body
Model 1B	B ($C_{10} = 3.4$ MPa, $D_1 = 0.029$ MPa^{-1})	Rigid body
Model 1C	C ($C_{10} = 3.4$ MPa, $D_1 = 0.003$ MPa^{-1})	Rigid body
Model 1D	D ($C_{10} = 6.8$ MPa, $D_1 = 0.0015$ MPa^{-1})	Rigid body
Model 2	A ($C_{10} = 2.043$ MPa, $D_1 = 0.051$ MPa^{-1})	Tie

Load When modeling one leg standing, a study by Bergmann et al. [72] that measured the hip contact forces was used. The contact force was measured in vivo using hip implants with telemetric data transmission. The forces were measured in the x-, y-, and z-direction in the femoral coordinate system. The hip contact forces were measured in four subjects aged 51 to 76 years old. The data from all four subjects were used by Bergmann et al. to define the load for an average subject of 75 kg in one-leg-stance [72]. This is the load that was used in the FE models of one leg standing. The load in all directions was scaled to correspond to the subject of 63 kg used in this thesis and ended in a load of 170 N, 1500 N, and 91 N, in the x-, y-, and z-direction, respectively. The load used for one leg standing represented the peak force when standing on one leg using the data from Bergmann et al. The forces were applied in the reference point in the center of the femoral head (see figure 3.10).

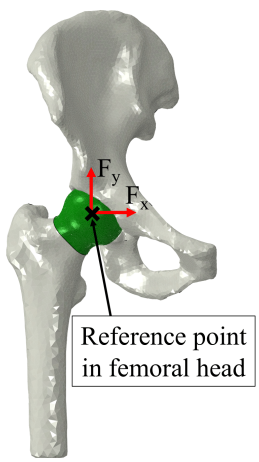

(a) Coronal view of the hip.

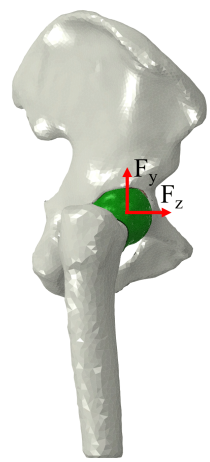

(b) Sagittal view of the hip.

(c) The reference point in the pelvis is located in the acetabulum.

Figure 3.10: The load was applied in the center of the femoral head. Subfigure a and b shows the direction of the forces and the center of the femoral head, where the boundary conditions of the femur were applied. Subfigure c show the reference point in the acetabulum.

Boundary conditions For the models using rigid body constraints, displacement/rotation boundary conditions were defined in the reference points of the femur and pelvis. The reference point of the femur

was located in the center of the femoral head (see figure 3.10), and the reference point in the pelvis was located in the acetabulum (see figure 3.10). The center of the femoral head was free to translate in all directions, but all rotations were constrained. The reference point in the acetabulum was fully fixed for all movements.

When tie constraints were used, coupling was also used. This meant that there was a reference point in the femoral head that could be used for assigning boundary conditions to the femur. In the center of the femoral head, the boundary conditions used were the same as when rigid body constraints were used. For the boundary conditions of the pelvis, two regions were assigned and fully fixed, both in translation and rotation. These regions included nodes along the pubis joint and iliac crest.

Walking

To further develop the model, the gait cycle was included. Different material parameters were compared and how ligaments affected the model were investigated to make the model more realistic. It resulted in a total of six models representing gait, as seen in table 3.5. Based on the results from the model of one leg standing, all the models including the gait cycle used rigid body constraints. Four of the models included different sets of material parameters for cartilage. The last two models both included ligaments in the hip joint, and two different options for boundary conditions were used. Material properties of articular cartilage ($C_{10} = 2.043$ MPa, $D_1 = 0.051$ MPa^{-1}) was the same for both FE models including ligaments.

Table 3.5: A summary of all models that simulated walking.

	Cartilage	**Ligaments**	**Allowed movements**
Model 3A	A	No	Flexion/extension
Model 3B	B	No	Flexion/extension
Model 3C	C	No	Flexion/extension
Model 3D	D	No	Flexion/extension
Model 4	A	Yes	Flexion/extension
Model 5	A	Yes	Flex./ext., Abd./add.

Load An average gait cycle, when walking at level ground at a speed of 3.5 km/h, lasts for 1.1 seconds and starts at heel strike [72]. To model the flexion and extension motion during the gait cycle, the femur was rotated around the reference point in the femoral head and the rotation angle varied over time. The maximum angle used was 25.1°and the minimum angle used was -11.1°[73]. The variation of the flexion/extension angle over the gait cycle can be seen in figure 3.11.

To model the gait cycle, forces from a person of 75 kg that is walking presented in the study by Bergmann et al. was used [72]. The force in x-, y-, and z-direction were used and varied during the gait cycle. The force in all directions was scaled to represent the weight of the subject (63 kg) (see figure 3.12). The maximum force was 1459 N, which is equal to approximately 236% of the body weight.

The analysis of all gait cycle models was divided into two steps. In the first step, the femur was rotated from its initial position to the angle at the start of the gait cycle, heel strike. Simultaneously, the initial force in all directions was applied. In the second step, the varying rotation and hip joint forces in the gait cycle were applied.

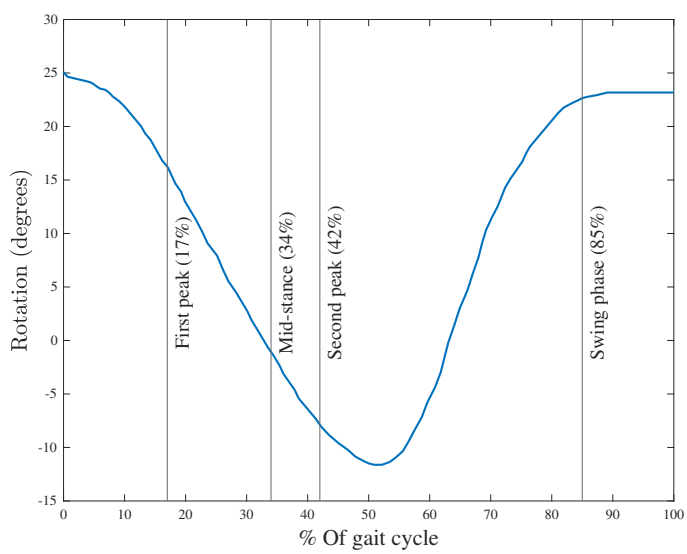

Figure 3.11: The flexion/extension angle in the hip joint in the gait cycle, starting at the heel strike. The vertical lines represent the first peak in the load curve, mid-stance, second peak, and the lowest load in the swing phase.

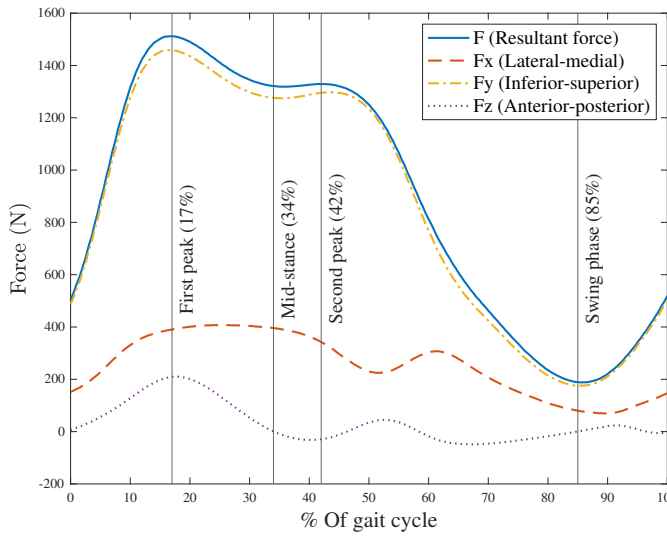

Figure 3.12: Resultant reaction force and its components during the gait cycle for the subject with a weight of 63 kg. The vertical lines represents the first peak, mid-stance, second peak, and the lowest load in the swing phase.

Boundary conditions Rigid body constraints were used for all models of the gait cycle and the boundary conditions were defined in the reference points in the center of the femoral head and in the acetabulum. The boundary conditions in the acetabulum were the same as for the one leg standing models, completely fixed in both rotation and translation. The boundary conditions in the femur were different from the one leg standing models as the walking models included rotation around the reference point. In the first version of the models, the reference point was free to translate in all directions and all rotations were constrained except for the flexion/extension motion, where rotation was applied. In the second version of the model, the center of the femoral head was only fixed for internal/external rotations, and otherwise free to move. The first option of boundary conditions was used for the models without ligaments and all four sets of material parameters for cartilage (model 3A-3D). It was also used for one of the models including ligaments (model 4). The second option of boundary conditions was used for the second model including ligaments (model 5).

Ligaments The ligaments included in the FE model were the three ligaments in the hip joint capsule. They were modeled using several spring elements in Abaqus, that connected nodes on the pelvis to nodes on the femur. Several nodes in the area where each ligament is attached were selected. Each ligament was modeled as 6-8 spring elements as done by Zou et al. [74]. The number of springs used for each ligament and the stiffness can be seen in table 3.6. Some of the ligaments included in the FE model can be seen in figure 3.13.

Table 3.6: Ligaments used in the FE model, number of spring elements, and stiffness of each spring element [74].

Ligament	Number of elements	Spring stiffness [N/mm]
Ischiofemoral	8	5
Pubofemoral	6	6
Inferior iliofemoral	6	17
Superior iliofemoral	6	16

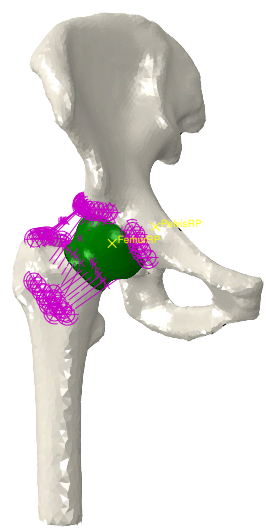

Figure 3.13: The model of the hip joint including ligaments. The reference point in the center of the femoral head and the reference point in the acetabulum are also visible in the figure.

3.5 Reconstruction of DXA images and scaling of the FE model

The focus of this section of the thesis was to use the DXA images with previously automatically annotated landmarks to reconstruct a femur with a similar shape. The FE model of the hip joint (model 5) was then scaled based on the reconstructed femur to finally predict the cartilage contact in the hip joint in the DXA image. An overview of the reconstruction of DXA images and scaling of the FE model can be seen in figure 3.14.

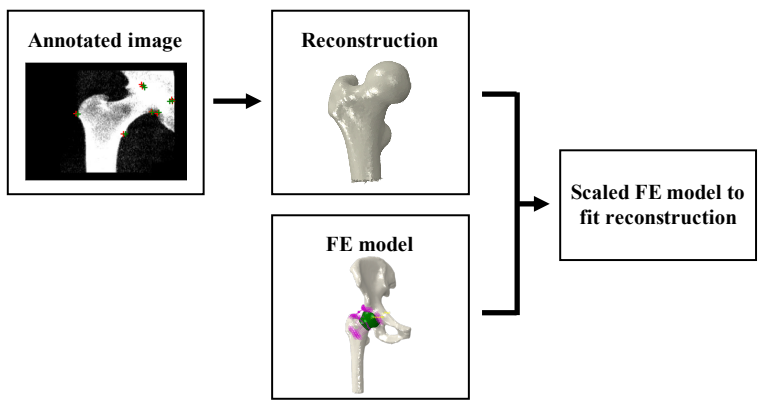

Figure 3.14: An overview of the reconstruction and scaling of the CT-based FE model.

The reconstruction of the femur based on the annotated DXA images was performed using a previously developed algorithm by Väänänen et al. [8]. The reconstruction algorithm is based on a statistical shape and appearance model (SSAM). It uses a number of DXA images of the femur to create a model of the mean shape plus a variation in a number of parameters. The reconstruction algorithm will take a simulated X-ray of the SSAM model and compare it to the DXA image and landmarks used as an input, change the variation slightly and compare it again. This will be repeated until convergence.

Nine DXA images with automatically detected landmarks were reconstructed. The images used were the three best predictions with the highest accuracy, the three worst, and the three in the middle. The images used were selected to compare how well the reconstruction would work in different grades of predicted landmarks. The landmarks in all nine of the images were predicted with the same trained sML-morph. To

evaluate the reconstructed femurs, both the manually annotated landmarks and the automatically detected landmarks were used. In total, 18 femurs were reconstructed.

To investigate the effect different grades of predictions had on the accuracy of the reconstruction, the reconstructions based on manually annotated landmarks and predicted landmarks were compared using CloudCompare [75]. The two meshes (prediction-based and manual-annotation-based) were aligned and the cloud-to-mesh distance was calculated. The cloud-to-mesh distance between the two meshes is the distance between a node on the prediction-based femur to anywhere on the manual-annotation-based femur (a node or a triangular element) [76].

FE models from reconstructions

The second step of this part of the thesis was to scale the FE model of the hip joint previously made to be of the same size as the reconstructed femur.

The reconstructed femurs were rotated and aligned to the femur in the CT-based FE model using CloudCompare [76]. The models were scaled in the x-, y-, and z-direction by finding a ratio between the reconstructed femur and the femur in the FE model. Two measurements on the proximal femur were used, made up of four points (see figure 3.15):

- **Point 1**: On the top front of the femoral head.
- **Point 2**: On the lower back of the greater trochanter.
- **Point 3**: On the posterior side of the femoral head, where the head meets the neck.
- **Point 4**: On the anterior side of the femoral head, where the head meets the neck, opposite to point 3.

The node number corresponding to each of the four points was manually picked in the meshes of the reconstructed femurs and the femur in the CT-based FE model. This was not possible to do automatically as the mesh of all the reconstructions was the same but the number of each node was not. The points used were chosen as they describe the shape of the entire proximal femur and, the most valuable part to this thesis, the femoral head.

The distance between the points in measurement 1 (point 1 and 2) and measurement 2 (point 3 and 4) for both the reconstructed femur and the FE model was calculated in all three directions. The distance in each direction of the two measurements in the reconstruction was then

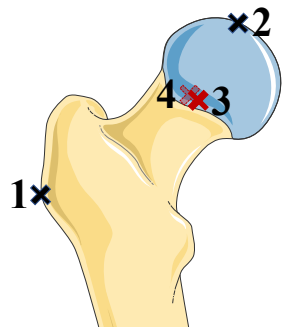

Figure 3.15: The four points used to obtain the ratios to scale the FE model of the hip joint. Point 3 is on the anterior side of the femoral head and point 4 is on the posterior side.

divided by the same distance in the FE model to obtain the ratios, one in each direction. In the x- and y-direction the final ratio was calculated as the mean of the ratios from the two measurements. In the z-direction, only the ratio from measurement 1 was used due to measurement 2 being parallel to the z-axis, making the distances in the z-directions close to zero and the ratios very large.

In each column of nodes in the Abaqus input file of the FE model, the coordinates of the femur, pelvis, acetabular cartilage, and femoral cartilage, respectively, were multiplied with the ratio of the corresponding axis. This acquired 18 FE models of the hip joint, scaled based on the geometry of each reconstruction. All loads applied in each scaled FE model were also adjusted to the weight of the subjects available in the MrOS study. The 18 scaled FE models were otherwise unchanged from the original FE model of the hip and run in Abaqus.

The difference in geometry between the femur in the scaled FE models based on reconstructions made from automatically detected landmarks and manually annotated landmarks was compared. This was done using CloudCompare. The femurs (prediction-based and manual-annotation-based) were aligned and then the cloud-to-mesh distance was calculated. This was done to evaluate the effect that the manually annotated landmarks compared to automatically detected landmarks had on the scaled shape of the femur.

Chapter 4

Results

4.1 Automatic landmark detection

The performance results of the different tests done with oML-morph and sML-morph will be presented in this section. This includes parameter space evaluation, data augmentation, variation of train-test data ratios, and robustness tests with radiography images. The parameter *ME* (mean of euclidean distance) and *MA* (mean of minimum, maximum and mean distance in the x-direction, y-direction, and euclidean distance) introduced in section 3.3.1 was use to evaluate the two ML-morph methods.

4.1.1 Improvement of the algorithm

The oML-morph made less accurate predictions compared to the sML-morph. On average and with equivalent parameters, the value of *MA* predicted with sML-morph was 25% more accurate than *MA* when using oML-morph.

The six best combinations of parameter sets and their performance can be seen in table 4.1. The set of parameters with the lowest accuracy gave predictions with a 67% larger deviation in total, that was a mean of 1.1 pixels per landmark compared to 0.68 pixels per landmark for the set that performed the best. The three best, three worst and three middle predictions for the very best set of parameters (set 4) can be seen in figure 4.1. The performance of each parameter is dependent on the other parameters and therefore it was difficult to determine their individual contributions. The parameter that made the largest differ-

ence to the performance, regardless of the value of the others was the Cascade depth. A cascade depth between 30-50 gave the most accurate results. Values below and above that worsened the accuracy.

Table 4.1: The six best combinations of parameters used in sML-morph as well as their performance. For all images, threads = 1, tree dept = 1, and feature pool size = 10 was used.

Set nbr	**Cascade depth**	μ	**Over-sampling**	**Deviation x-direction [pixels]**	**Deviation y-direction [pixels]**	***MA* [pixels]**	***MA*/*MA*(4)**
1	50	0.02	100	3.15	2.06	9.13	1.67
2	50	0.02	10	3.22	2.03	8.51	1.55
3	30	0.02	200	3.09	1.97	6.37	1.16
4	50	0.02	200	2.99	1.83	5.48	1.00
5	50	0.1	10	3.29	2.07	8.37	1.53
6	50	0.05	10	3.25	2.03	7.20	1.32

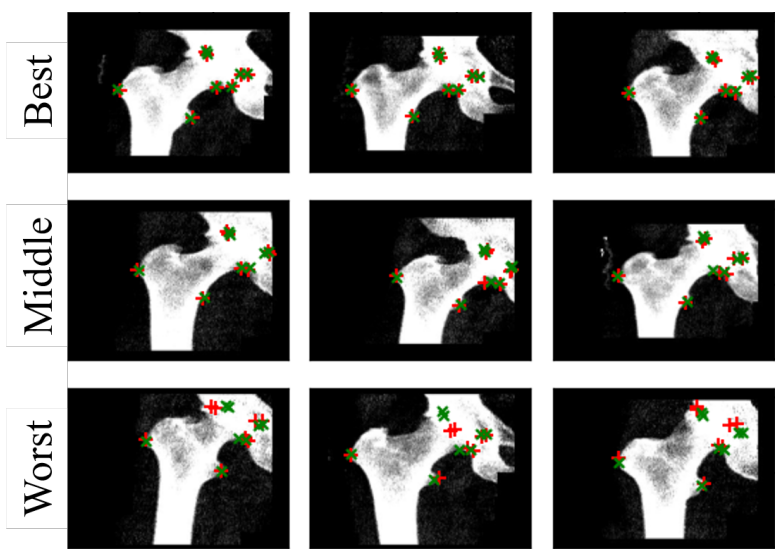

Figure 4.1: The best, middle, and worst predictions for sML-morph run with the best set of parameters (set 4). Red plus (+) was manual annotations and green cross (×) was predicted.

The performance histograms for each of the six best sets of parameters can be seen in figure 4.2. The general distribution was centered around the peak and only a few outliers were present. It was also visible that all

predictions had a similar distribution with a high peak of approximately five pixels.

Some parameters also had a larger impact on the time it took to do the training. The computational cost scales with the oversampling parameter which made set 2, 3, and 4 take approximately ten times longer to train than parameter set 1, 5, and 6.

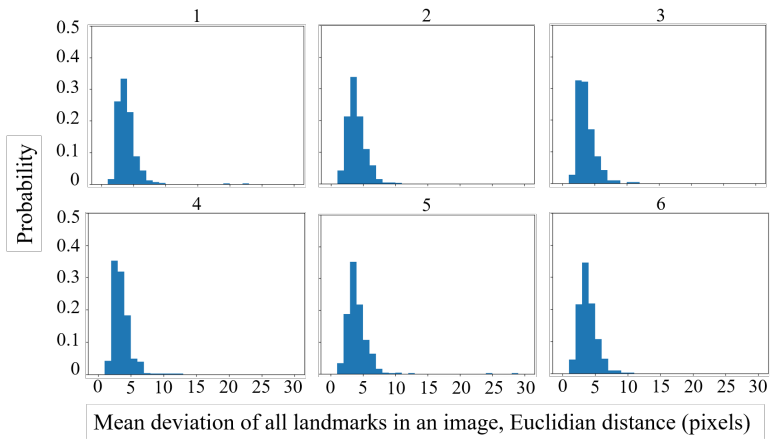

Figure 4.2: Histograms of the mean deviation using the six best sets of parameters.

4.1.2 Attempts to improve the accuracy

The results from masking, rotating the images, and removing landmarks are presented below.

Masking

The masked images gave predictions where *ME* was 8.4% worse than in the original DXA images and *MA* was 5.3% worse. The double-masked images gave predictions where *ME* was 1.5% worse and *MA* was 35% worse.

Rotating the images

When doing the parameter testing on oML-morph, a larger deviation in the x-direction (lateral-medial) was observed. *ME* was up to 59% larger in the x-direction than in the y-direction with a mean difference of

43%. A comparison of the results for the original images and the rotated images can be seen in table 4.2. oML-morph had a smaller difference in the deviation in the x- and y-direction compared to sML-morph when using non-rotated images. It was also possible to see that the rotated images gave far larger differences in the x-direction compared to the y-direction than the non-rotated ones for both oML-morph and sML-morph.

Table 4.2: Deviation in the x-direction compared to the y-direction of rotated images and non-rotated images for sML-morph and oML-morph.

	Non-rotated simple (x/y)	**Non-rotated original (x/y)**	**Rotated simple (y/x)**	**Rotated original (y/x)**
Mean of *ME*	1.63	1.42	3.51	5.99
Max of *ME*	1.66	1.40	3.85	6.07
Mean of *MA*	1.26	1.33	3.79	6.93

Removing landmarks

The oML-morph method had some variation when predicting the different landmarks as can be seen in figure 4.3 that shows the performance histograms for the prediction of each of the individual landmarks. It showed that landmark 1 and 2 were better predicted than landmark 3-8. When any of the ML-morph methods (sML-morph or oML-morph) were used to predict different groups of landmarks, the results were generally worse with the exception of landmark 1 and 2, which performed 10% better (see table 4.3). Therefore, it was decided to keep the prediction of all landmarks at once, instead of splitting and doing the prediction in several steps.

Different ratios of train and test

The performance of sML-morph using different ratios of images to do training and to test it can be seen in table 4.4. There was a pattern where the mean value of *MA* was higher when a larger portion of the images were used for training, except for when 60% were used.

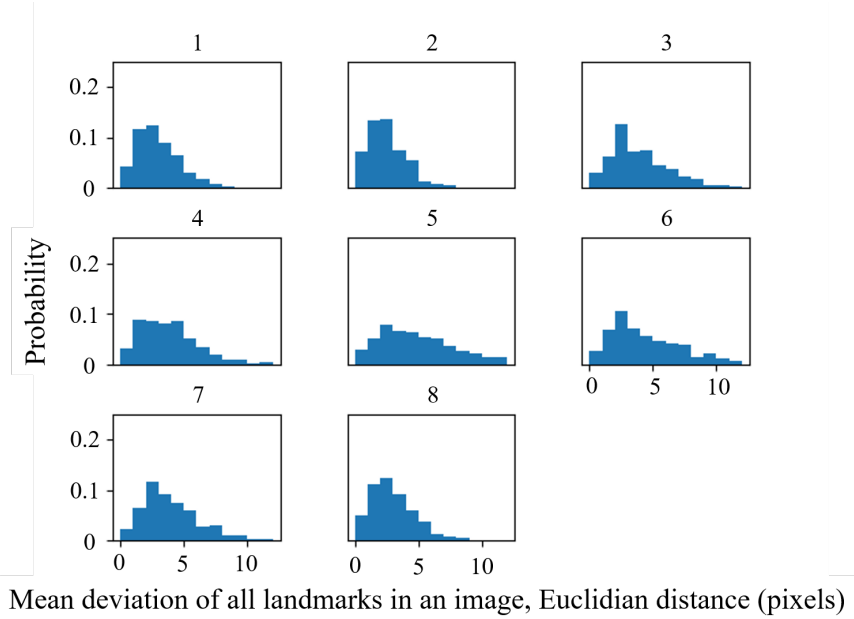

Figure 4.3: Histogram of prediction of the different landmarks.

Table 4.3: The performance of different sets of landmarks.

Landmarks included	**Mean of *MA* [pixels]**	**Mean of *MA* for landmarks included / mean of *MA* for all landmarks**
All	5.84	1.00
1,2,3,4	7.15	1.22
5,6,7,8	53.04	9.08
1,3,5,7	37.58	6.43
2,4,6,8	54.95	9.41
1,2	5.25	0.90
3,4,5,6,7,8	62.10	10.63

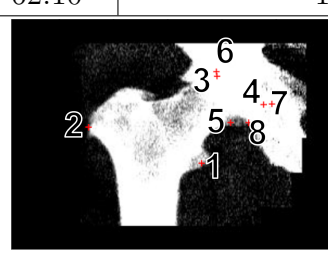

Table 4.4: Performance of different ratios of images in the test set and the training set. Also compared to the ratio used in the rest of the thesis (0.8).

Ratio of images in the training set	**Mean of *MA* [pixels]**	**Compared to *MA*(0.8)**
0.5	13.39	1.75
0.6	4.59	0.60
0.8	7.66	1.00
0.9	5.80	0.76
0.95	3.90	0.51
0.99	3.20	0.42

4.1.3 Robustness to other types of images

Using only the 205 radiography images, the predictions had a low accuracy compared to using all of the DXA images. When mixing the two, the performance increased compared to when only the radiography images were used, but the predictions of the DXA images became less accurate (see table 4.5). An example of a prediction of a radiography image can be seen in figure 4.4, where sML-morph was trained on both DXA and radiography images.

Table 4.5: Deviation of predictions in radiography images compared to DXA images, annotated using sML-morph.

	DXA images	**Mix of DXA and Radiography images**	**Radiography images**
ME [pixels]	4.21	5.77	26.00
MA [pixels]	4.75	19.07	29.28
MA/ *MA* of DXA	1.00	4.01	6.16

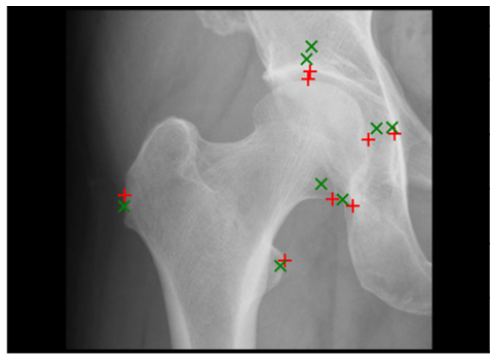

Figure 4.4: Radiography image with predicted landmarks made by sML-morph trained on a mix between radiography images and DXA images. Red plus (+) are manual annotations and green crosses (×) are predictions.

4.2 CT-based FE model of the hip joint

Firstly, the results for the five FE models of standing are presented and secondly, the results from the six models including walking are presented.

4.2.1 One leg standing

First, the results from the comparison of the two types of constraints used, rigid body and tie constraints (model 1A and 2), are presented. Then, the results for when different material parameters for cartilage were used (model 1A-1D).

When comparing the two models that evaluated the effect of including deformable bones (model 1A and 2), the maximum contact pressure, the maximum von Mises stress, the maximum major principal strain, and run time were compared. When tie constraints were used (model 2), the maximum contact pressure was approximately 2.0% lower compared to when rigid body constraints were used, the maximum von Mises stress was 7.5% higher, and the maximum major principal strain was 13% higher (see table 4.6). The run time when using tie constraints was 54% longer compared to when rigid body constraints were used.

Table 4.6: Maximum contact pressure, maximum von Mises stress, and maximum major principal strain in the acetabular cartilage, as well as the run time for the models of one leg standing using rigid body constraints (model 1A) and tie constraints (model 2). Cartilage A ($C_{10} = 2.043$ MPa, $D_1 = 0.051$ MPa^{-1}) was used in both of the models.

	Maximum contact pressure [MPa]	**Maximum von Mises stress [MPa]**	**Maximum major principal strain**	**Time [sec]**
Model 1A	2.47	1.47	0.08	590
Model 2	2.42	1.58	0.09	911

The four models that used different material parameters (model 1A-1D) were compared by studying the contact pressure (see figure 4.5), the von Mises stress (see figure 4.6), and the major principal strain (see figure 4.7), in the acetabular cartilage. Overall, the results for model 1A and 1B were similar, and model 1C and 1D were similar. The most visible difference could be seen between model 1A and 1D for both contact pressure, von Mises stress, and major principal strain.

Model 1A-1D were also compared by studying the maximum values of the contact pressure, the von Mises stress, and the major principal strain (see table 4.7). The largest difference in maximum contact pressure between the models was 3.6% when comparing models 1A and 1D. Both the maximum von Mises stress and the maximum major principal strain were decreasing as a stiffer cartilage was used. The maximum von Mises stress was 18% lower in model 1D compared to model 1A and the maximum major principal strain was 63% lower in model 1D.

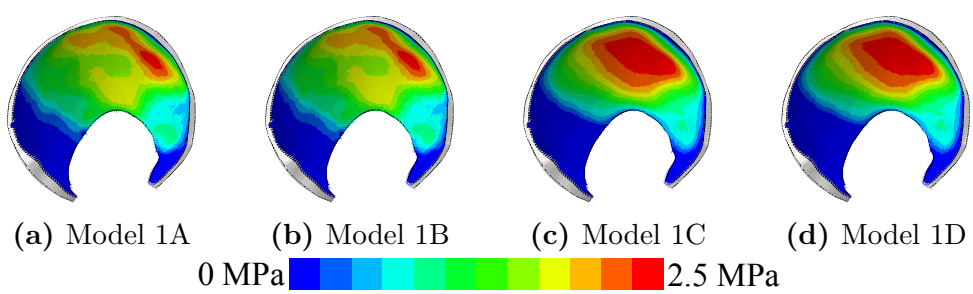

Figure 4.5: Contact pressure [MPa] in the acetabular cartilage in the model of one leg standing using rigid body constraints and all four sets of material parameters for cartilage (A-D).

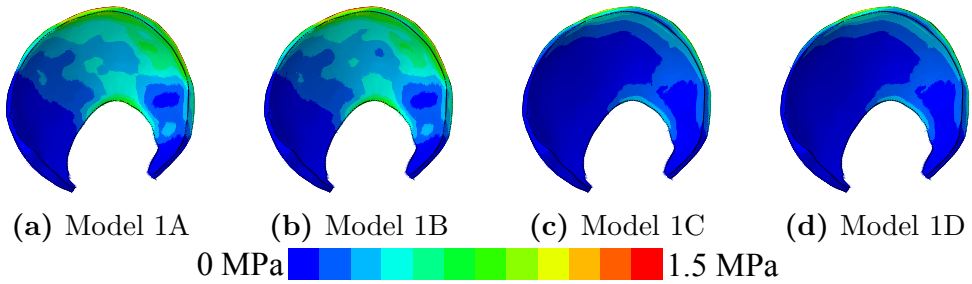

Figure 4.6: Von Mises stress [MPa] in the acetabular cartilage in the model of one leg standing using rigid body constraints and all four sets of material parameters for cartilage (A-D).

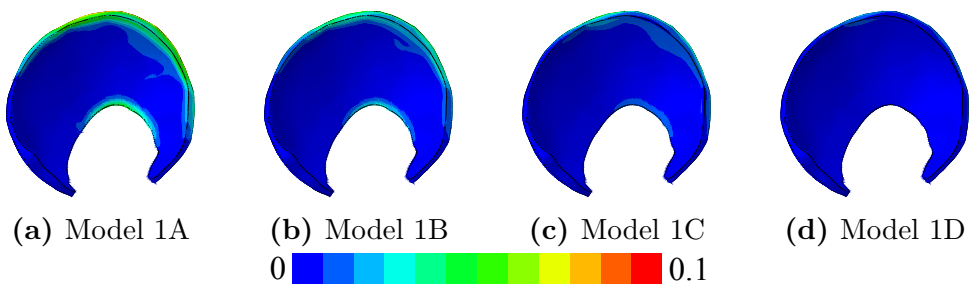

Figure 4.7: Major principal strain in the acetabular cartilage in the model of one leg standing using rigid body constraints and all four sets of material parameters for cartilage (A-D).

Table 4.7: Maximum contact pressure, maximum von Mises stress, and maximum major principal strain for the models of one leg standing with the four sets of material parameters for cartilage (A-D).

	Maximum contact pressure [MPa]	**Maximum von Mises stress [MPa]**	**Maximum major principal strain**
Model 1A	2.47	1.47	0.08
Model 1B	2.48	1.46	0.05
Model 1C	2.56	1.20	0.05
Model 1D	2.56	1.21	0.03

4.2.2 Walking

The results for the models of walking begin with the ones that used the different material parameters for cartilage (model 3A-3D). Additionally, the models that included ligaments (models 4 and 5) are presented and compared to model 3A. Model 3A, 4, and 5 all used the same material parameters for cartilage (Cartilage A: $C_{10} = 2.043$ MPa, $D_1 = 0.051$ MPa^{-1}). All results for the models of walking are presented at four time points in the gait cycle: the first peak of the load curve, mid-stance, second peak, and at the lowest load in the swing phase. These time points corresponds to 17%, 34%, 42%, and 85% of the gait cycle (see figure 3.12).

Model 3A-3D was compared to each other by studying the contact pressure, the von Mises stress, and the major principal strain in the acetabular cartilage. By studying the pattern of the contact pressure in figure 4.8 it can be seen that it was changing between the four time points of the gait cycle (first peak, mid-stance, second peak, and swing phase). Both the pattern and the location of the contact pressure were changing when the load and the flexion/extension angle changed. Differences in the contact pattern between the models with different material parameters can also be seen in the figure. The changes in contact pattern over the gait cycle were similar between the models. However, at the first peak (upper left in each subfigure), a notable difference in how large the area that was in contact can be seen. The contact area decreased when a stiffer material was used, but the area with the values in the higher part of the spectrum, or above the limit of 8 MPa, increased.

Not only did the contact pattern change over the gait cycle, and between the four models, there was also a change in the maximum contact pressure (see table 4.8). In all of the four time points, the maximum contact pressure was increasing when a stiffer material was used, where cartilage D was the stiffest. When comparing model 3A and 3D, the maximum contact pressure was 160% higher in model 3D at the first peak. At the three other time points, the maximum contact pressure was 180%, 260%, and 96% higher in model 3D compared to model 3A.

By instead evaluating the difference in the von Mises stress in model 3A-3D (see figure 4.9), it can be seen that values in the higher part of the spectrum ($\approx$ 8 MPa or higher) were not present in model 3A. Especially by studying the first peak (upper left in each subfigure) in all four models, it can be seen that using a stiffer cartilage was leading

to higher von Mises stress, and the highest values can be found at the first peak. When comparing model 3A and 3D, the maximum von Mises stress was 160%, 180%, 240%, and 110% higher in model 3D at the four different time points (see table 4.9).

Table 4.8: Maximum contact pressure [MPa], for all models of the gait cycle, at the first peak of the load curve, mid-stance, second peak, and at the lowest load in the swing phase.

	First peak	**Mid-stance**	**Second peak**	**Swing phase**
Model 3A	11.7	3.16	6.28	5.74
Model 3B	16.6	4.05	10.5	7.32
Model 3C	23.2	5.47	13.5	8.10
Model 3D	30.5	8.85	22.7	11.2
Model 4	11.1	3.16	6.51	6.67
Model 5	11.2	3.08	6.89	4.62

Table 4.9: Maximum von Mises stress [MPa], for all models of the gait cycle, at the first peak, mid-stance, second peak, and in the swing phase.

	First peak	**Mid-stance**	**Second peak**	**Swing phase**
Model 3A	9.13	1.60	4.45	4.38
Model 3B	13.2	2.01	7.27	5.44
Model 3C	17.9	2.62	9.31	6.14
Model 3D	23.3	4.42	15.3	9.39
Model 4	8.77	1.60	4.49	7.35
Model 5	8.19	1.82	4.76	11.6

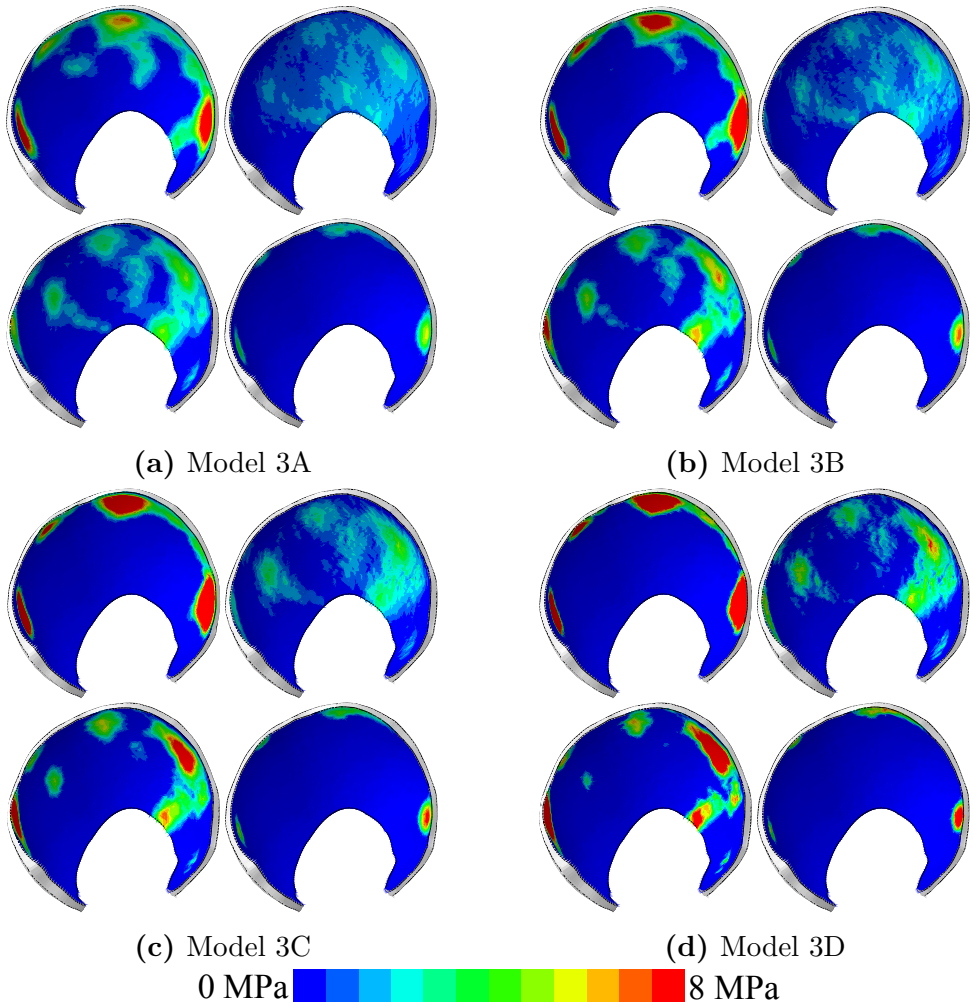

(a) Model 3A **(b)** Model 3B

(c) Model 3C **(d)** Model 3D

Figure 4.8: Contact pressure [MPa] in the acetabular cartilage in the model including the gait cycle. Each subfigure shows a model that used one of the four sets of material parameters for cartilage (A-D). The upper left figure in each subfigure represents the first peak in the load curve, the upper right is the mid-stance, the lower left is the second peak and the lower right is at the lowest load in the swing phase.

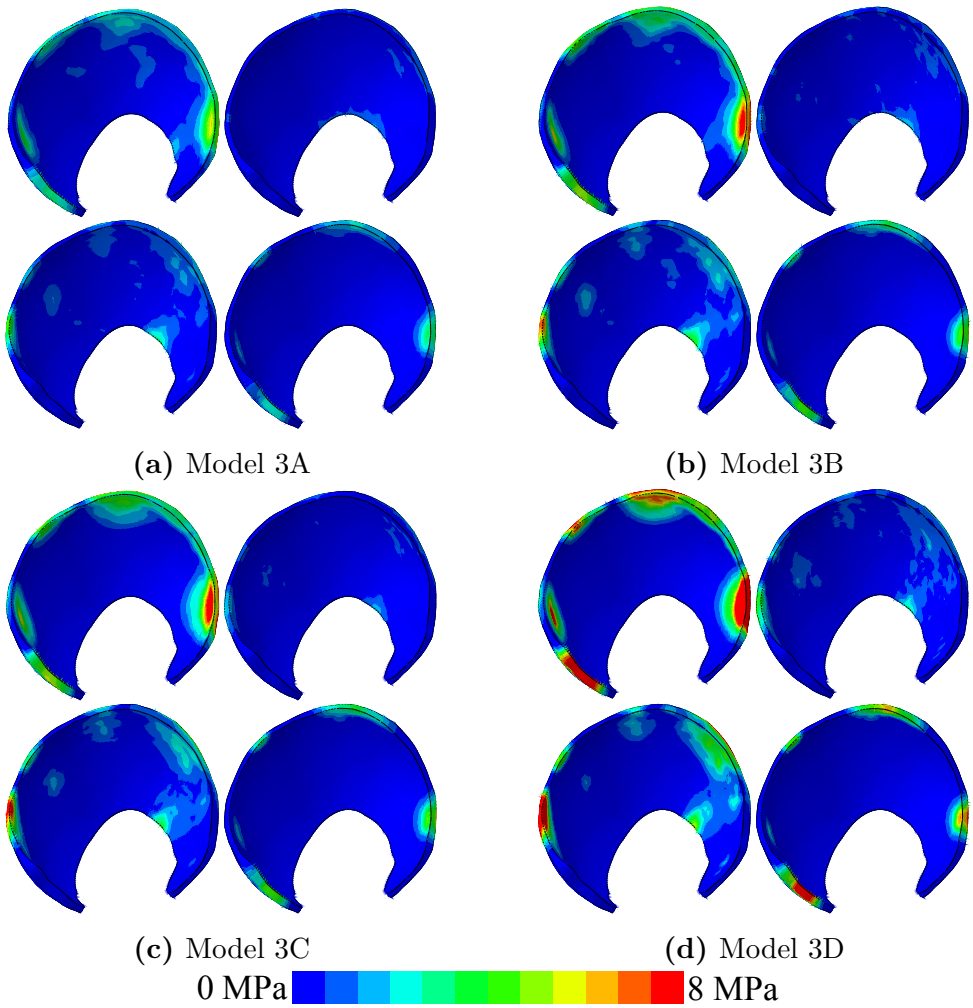

Figure 4.9: Von Mises stress [MPa] in the acetabular cartilage in the model including the gait cycle. Each subfigure shows a model that used one of the four sets of material parameters for cartilage (A-D). The upper left figure in each subfigure represents the first peak, the upper right is mid-stance, the lower left is the second peak, and the lower right is at the lowest load in the swing phase.

The last results produced for the models comparing the four sets of material parameters (model 3A-3D) were the major principal strains. By visually comparing the major principal strain in the acetabular cartilage seen in figure 4.10, there was no pattern that showed how it changed as a more stiff material was used. This was more distinct as the maximum values for the models were compared (see table 4.10). The difference was the largest between models 3B and 3C, and the maximum major principal strain was 70% higher at the first peak in model 3C.

Table 4.10: Maximum major principal strain, for all models of the gait cycle, at the first peak of the load curve, mid-stance, second peak, and swing phase.

	First peak	**Mid-stance**	**Second peak**	**Swing phase**
Model 3A	0.35	0.09	0.22	0.21
Model 3B	0.33	0.07	0.22	0.17
Model 3C	0.56	0.11	0.34	0.24
Model 3D	0.41	0.09	0.29	0.18
Model 4	0.34	0.09	0.22	0.53
Model 5	0.33	0.10	0.24	0.73

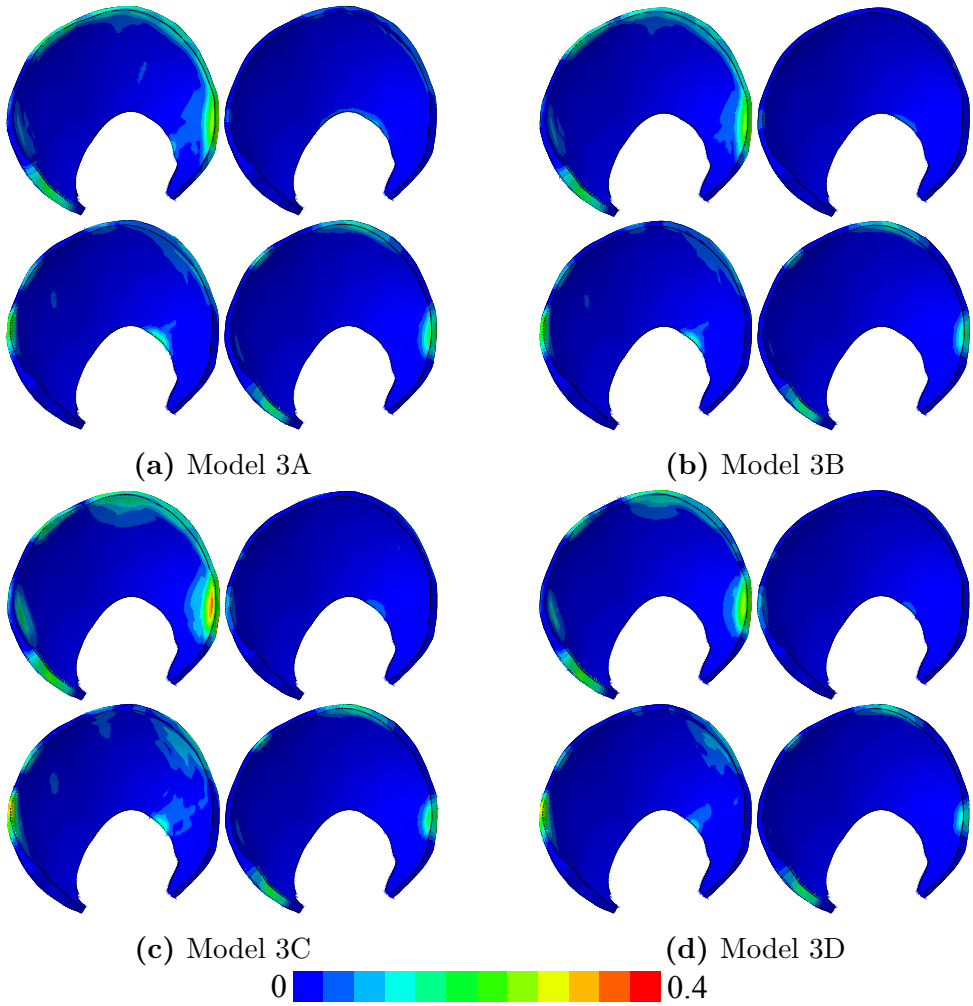

Figure 4.10: Major principal strain in the acetabular cartilage in the model including the gait cycle. Each subfigure shows a model that used one of the four sets of material parameters for cartilage (A-D). The upper left figure in each subfigure represents the first peak, the upper right is mid-stance, the lower left is the second peak, and the lower right is at the lowest load in the swing phase.

The results for the models that included ligaments (models 4 and 5) were compared to model 3A by looking at the translation in the center of the femoral head, the maximum contact pressure, the maximum von Mises stress, the maximum major principal strain, and lastly the reaction force in the reference point in the acetabulum.

The translation in the center of the femoral head for model 3A and 4 was overall more similar in all directions compared to model 5 (see figure 4.11, 4.12 and 4.13). The difference in translation between the models was larger in the inferior-superior direction and the anterior-posterior direction, and was the largest at 85% of the gait cycle.

At the first peak of the load curve the maximum contact pressure in model 4 was 4.7% lower compared to model 3A, and model 5 was 4.3% lower (see table 4.8). At mid-stance, models 3A and 4 gave the same maximum contact pressure, and model 5 was 2.5% lower. At the second peak, the maximum contact pressure in model 4 was 3.7% higher compared to model 3A, and in model 5 it was 9.7% higher. In the swing phase, the difference between the models was more prominent and was 16% higher in model 4, and 20% lower in model 5, compared to model 3A. The von Mises stress and the maximum major principal strain also followed the pattern that the first peak, mid-stance, and second peak were similar while the difference was larger in the swing phase (see table 4.9 and 4.10). The difference in the maximum von Mises stress between the models at the first peak, mid-stance, and the second peak ranged from 0-12%. At the swing phase, model 4 had a maximum von Mises stress that was 68% higher compared to model 3A, and 170% higher for model 5. The difference in maximum major principal strain ranged from 0-11%, at the first peak, mid-stance, and at the second peak. The difference at the swing phase was as large as 150% for model 4, and 250% for model 5, compared to model 3A.

The last result for the CT-based FE models was the reaction force in the reference point in the acetabulum, presented in figure 4.14. The reaction force was the same for both models 3A, 4, and 5, and can be seen in figure 3.12.

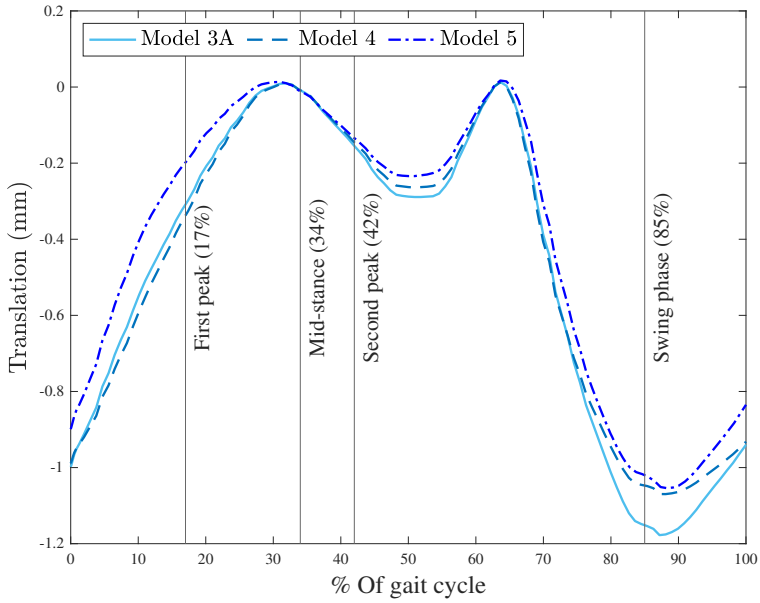

Figure 4.11: Translation [mm] in the lateral-medial direction in the reference point in the center of the femoral head for model 3A, 4, and 5.

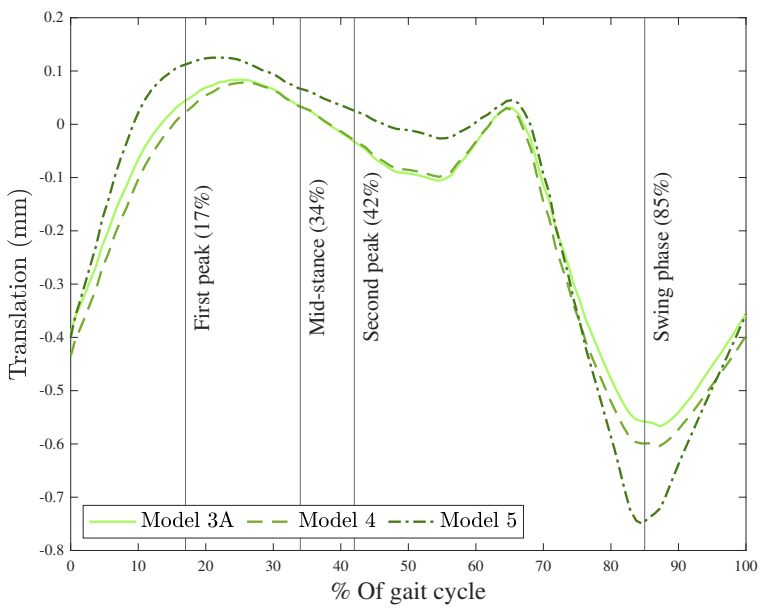

Figure 4.12: Translation [mm] in the inferior-superior direction in the reference point in the center of the femoral head for model 3A, 4, and 5.

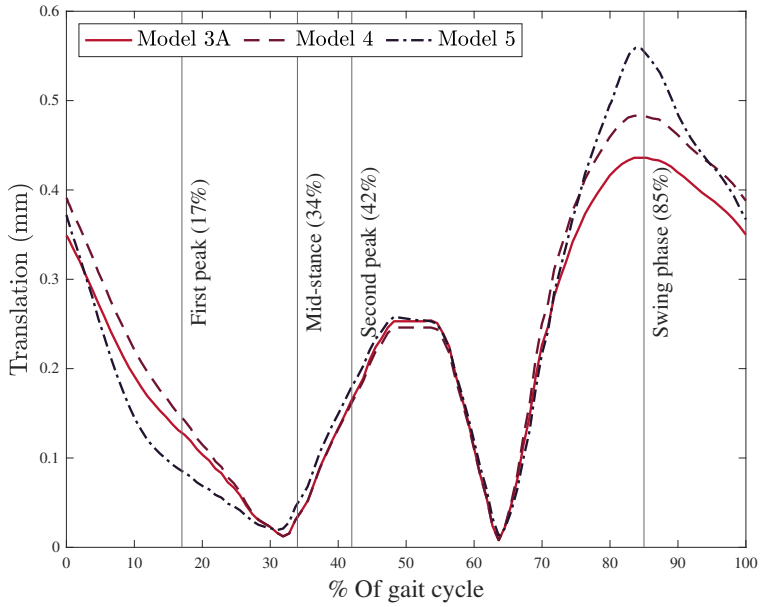

Figure 4.13: Translation [mm] in the anterior-posterior direction in the reference point in the center of the femoral head for model 3A, 4, and 5.

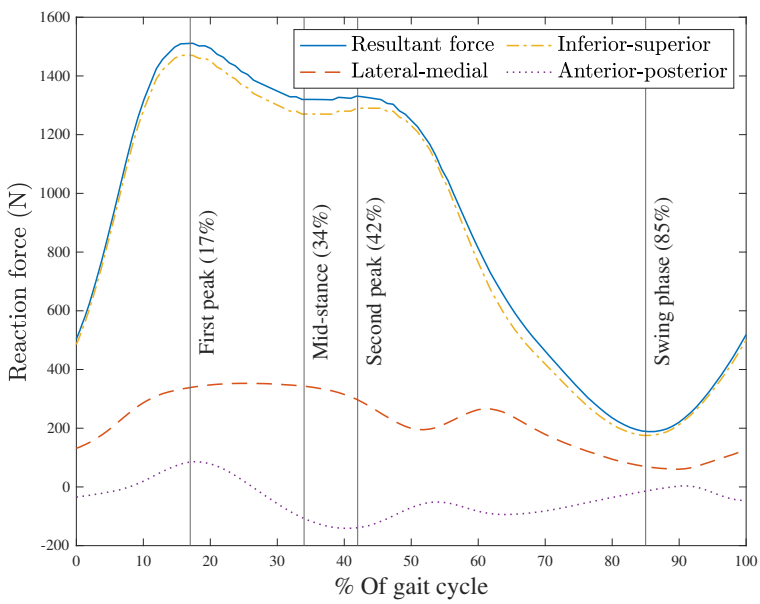

Figure 4.14: Reaction forces [N], all components and resultant force, in the reference point in the acetabulum over the gait cycle. The reaction force was the same for both model 3A, 4, and 5.

4.3 Reconstruction of DXA images and scaling of FE model

The results of reconstructing the 3D models of the femur based on manually annotated landmarks and automatically detected landmarks in DXA images are presented in this section. Results of the scaled FE models based on the reconstructions are also presented.

Nine of the DXA images predicted using automatic landmark detection were used for reconstruction, the three best predictions, three worst predictions, and three in the middle (figure 4.1). For all images, both the manually placed landmarks and the predicted landmarks were used to reconstruct a femur.

The mean cloud-to-mesh distance and the standard deviation between the reconstructions based on manually annotated and predicted landmarks differed between the images used (table 4.11), but the mean of the absolute values of the mean distances was very similar for each group of images. In the three best predictions, it was 0.67 mm, in the middle three it was 0.70, and in the worst three it was 0.70. In the worst three, the meshes for the automatic annotation based reconstructions were all smaller than the manual annotation based ones while both the best three and the middle three were generally larger. A visualization of the cloud-to-mesh distances for the nine sets of reconstructed images can be seen in figure 4.15. It is possible to see that the largest differences were in the femoral head with some variation in the top of the greater trochanter and in the lesser trochanter.

Table 4.11: Cloud-to-mesh distance for reconstructions based on the manual annotations and the predictions.

	Mean distance [mm]	**Standard deviation [mm]**
Best 1	0.86	1.34
Best 2	-1.10	0.98
Best 3	0.04	0.28
Middle 1	0.51	1.03
Middle 2	-0.26	0.69
Middle 3	1.33	1.22
Worst 1	-0.45	0.66
Worst 2	-1.28	1.37
Worst 3	-0.36	0.85

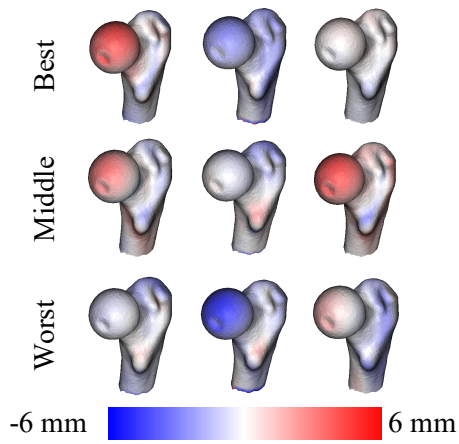

Figure 4.15: Visualization of the cloud-to-mesh distances between the reconstructed femurs based on automatically detected landmarks and manually annotated landmarks. Blue regions represents parts where the predictions were smaller than the manually annotated ones and red regions where they were larger.

4.3.1 Scaling the FE models

The ratios between the reconstructed femurs and the femur in the CT-based FE model ranged from 0.86-1.24 in the x-direction, 0.77-1.25 in the y-direction, and 0.86-1.17 in the z-direction (see table 4.12). Most of the reconstructions had a similar ratio in all three directions, but some stood out and had a more deviant ratio in one direction.

The mean cloud-to-mesh distance between the femurs in the scaled models varied (see table 4.13). The mean of the absolute values of the mean distances varied more between the grades of predictions when comparing the scaled femurs to each other. For the three best predictions it was 1.07, for the three in the middle it was 1.51, and for the three worst it was 1.09. A visualization of the cloud-to-mesh distance for each of the nine predicted images can be seen in figure 4.16 where it is clear that the scaled femurs had the largest differences in the femoral head and that the models based on prediction were generally smaller than those based on manually annotated landmarks.

Table 4.12: The ratios between the reconstructed femurs and the femur in the CT-based FE model in the x-, y-, and z-direction.

	x	**y**	**z**
Best 1 (manual)	1.24	1.22	1.17
Best 1 (predicted)	1.24	1.25	1.04
Best 2 (manual)	0.95	0.95	0.98
Best 2 (predicted)	1.09	0.77	0.86
Best 3 (manual)	1.00	1.00	0.95
Best 3 (predicted)	1.01	0.97	0.92
Middle 1 (manual)	1.03	1.05	1.12
Middle 1 (predicted)	0.99	0.97	0.96
Middle 2 (manual)	1.08	1.11	1.04
Middle 2 (predicted)	1.00	1.04	1.02
Middle 3 (manual)	0.96	1.05	0.93
Middle 3 (predicted)	0.93	0.95	0.90
Worst 1 (manual)	0.98	0.97	0.94
Worst 1 (predicted)	0.86	0.84	0.90
Worst 2 (manual)	1.05	1.13	1.02
Worst 2 (predicted)	1.06	1.16	1.04
Worst 3 (manual)	1.00	1.08	1.12
Worst 3 (predicted)	1.00	1.06	1.04

13 out of the 18 scaled FE models of the hip joint were completed, from which five pairs of models using manual and predicted landmarks were obtained (Best 3, Middle 1, Middle 2, Worst 1, and Worst 3). For these models, the maximum contact pressure in the acetabular cartilage at the first peak of the load curve was analyzed (see table 4.14). The difference in percentage between the scaled FE models based on predicted landmarks and manual landmarks was the lowest for Best 3, where the difference was only 1.7%. The highest difference was in Worst 3 which had a 20% difference in the maximum contact pressure.

The contact pressure for the five sets of models that were completed can be seen in figure 4.17. The contact pressure for the two models of Best 3 (manual and predicted) were similar, whereas Middle 1, Worst 1, and Worst 3 varied in a non systematic way.

Table 4.13: Cloud-to-mesh distance for the femurs scaled based on the manually annotated landmarks and the automatically detected landmarks.

	Mean distance [mm]	**Standard deviation [mm]**
Best 1	-0.47	1.31
Best 2	2.38	2.02
Best 3	-0.39	0.41
Middle 1	-1.94	1.42
Middle 2	-1.27	1.03
Middle 3	-1.31	0.93
Worst 1	-2.26	1.74
Worst 2	0.53	0.51
Worst 3	-0.50	0.83

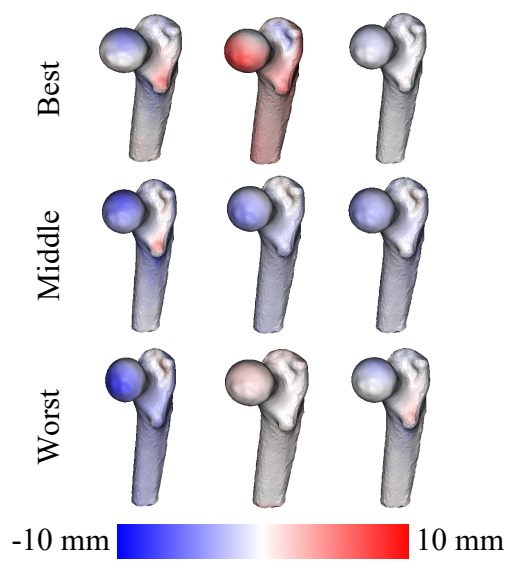

Figure 4.16: Visualization of the cloud-to-mesh distances between the scaled FE models based on automatically detected landmarks and manually annotated landmarks. Blue regions represents parts where the predictions are smaller than the manually annotated ones and red regions where they were larger.

Table 4.14: Maximum contact pressure at the first peak in the gait cycle for all reconstructed and scaled FE models.

	Maximum contact pressure [MPa]	**Difference between manual and predicted [%]**
Best 1 (manual)	12.45	Not complete
Best 1 (predicted)	Error	
Best 2 (manual)	11.08	Not complete
Best 2 (predicted)	Error	
Best 3 (manual)	13.46	1.7
Best 3 (predicted)	13.69	
Middle 1 (manual)	12.34	12.6
Middle 1 (predicted)	13.89	
Middle 2 (manual)	12.97	2.4
Middle 2 (predicted)	13.28	
Middle 3 (manual)	Error	Not complete
Middle 3 (predicted)	14.43	
Worst 1 (manual)	14.27	-3.7
Worst 1 (predicted)	13.74	
Worst 2 (manual)	Error	Not complete
Worst 2 (predicted)	Error	
Worst 3 (manual)	11.45	20.9
Worst 3 (predicted)	13.84	

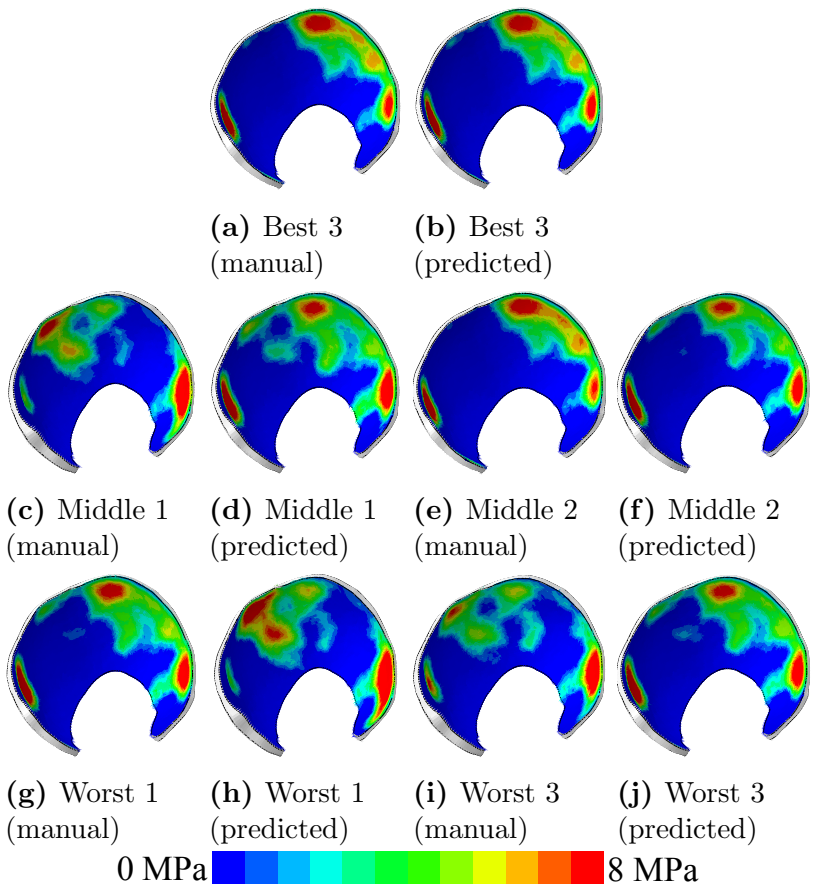

(a) Best 3 (manual) **(b)** Best 3 (predicted)

(c) Middle 1 (manual) **(d)** Middle 1 (predicted) **(e)** Middle 2 (manual) **(f)** Middle 2 (predicted)

(g) Worst 1 (manual) **(h)** Worst 1 (predicted) **(i)** Worst 3 (manual) **(j)** Worst 3 (predicted)

Figure 4.17: Contact pressure [MPa] in the acetabular cartilage at the first peak of the load curve (17%) for all the reconstructed and scaled FE models that were completed in pairs.

Chapter 5

Discussion

This thesis aimed to develop and evaluate tools that potentially can be used to assess hip deformities that occur during childhood. Methods to automatically detect anatomical landmarks in DXA images of the hip was evaluated, and FE models of the cartilage contact in the hip joint was developed. Together, the tools can be combined to automatically obtain 3D FE models of the hip joint from DXA images. A first implementation of this combined approach was made in the thesis.

5.1 Automatic landmark detection

The results from the investigation of the parameter space showed that it was possible to use ML-morph to predict the position of landmarks in a DXA image of the hip with a mean deviation of 0.68 pixels per landmark as can be seen in figure 4.1.

5.1.1 ML-morph

The performance metric used for ML-morph was based on pixels, which were 1.05 mm in the x-direction (lateral-medial) and 0.60 mm in the y-direction (inferior-superior). This gave a mean deviation in the x-direction of 0.22 mm per landmark and in the y-direction 0.24 mm per landmark. A combined accuracy in the x- and y-direction is thus 0.33 mm. As the thickness of healthy articular cartilage is 2-4 mm, the prediction requires high accuracy to be reliable. A difference of 0.33 mm per landmark is quite low compared to healthy adult cartilage thickness, but as the final application is to use it on pathological children,

the accuracy should be as high as possible. One of the ways to make this error smaller is to improve the resolution of the images. If the resolution is higher, the error in pixels that is allowed to obtain as accurate of predictions can be higher. The effects of having images with a higher resolution have not been investigated and would be an interesting approach to keep researching.

The performance of the ML methods was based on the difference between automatically detected landmarks and manually annotated landmarks. One question that this raised is whether the manual annotations are always correctly placed. As the manual annotations were made by hand there is a possibility of human error. The ML-morph method is more consistent and does not become tired or biased. As can be seen in figure 4.1 two of the worst images had landmarks in the manual annotations that were far from where they should be, particularly landmark 3 and 6. This gave lower *MA* and *ME* and was therefore considered less accurate while the predictions were more correct. This is important to keep in mind when analyzing the performance. The annotations were done by only one person which is also a possible mean of error. If all the images were independently annotated by several people at different times, the effect of the human error could be reduced and it could be more accurate to the anatomy.

Another aspect that can improve ML-morph is to have a larger train-to-test ratio. As seen in table 4.4, the accuracy became higher with more images in the training set. One outlier in that result was when using 60% to train sML-morph. Which of the images that were used for training and testing made a big impact on the parameter *MA* and *ME* when evaluating the performance, and very lucky splits could be the cause of this. The reason that one split could give *MA* and *ME* of higher accuracy is because some images, regardless of the performance, will have predictions with low accuracy as they look different from the others. The inaccuracies were thus because of limitations in the evaluation and not in the predictions. Images can be harder to use for prediction if they contain more of the pelvis, artifacts or noise, or if the manually annotated landmarks are in the wrong location. If a lot of images with annotations of lower accuracy or images that can be hard to predict are used for training, the errors will not affect the results and the value of *MA* and *ME*. The same split of testing and training data was therefore used for the entirety of the investigation of the parameter space.

The deviation in the x-direction compared to the deviation in the

y-direction was larger in sML-morph than in oML-morph, which would suggest that the oML-morph is better, but as the actual distances were smaller in sML-morph (sML-morph was 25% better), *MA* and *ME* were lower. As the deviation was larger in the y-direction than in the x-direction for the rotated images, it is hard to make a conclusion of which of the ML-morph methods handled the different deviations the best and it is likely that it depends on the images used.

When using the masked images, *ME* was 8.4% less accurate compared to when the original DXA images were used. When using the double-masked images, *ME* was 1.5% less accurate compared to the original DXA images. This showed that the performance of the three versions of images was similar and that more extensive testing would be needed to see if it improved the accuracy or not.

In conclusion, it is possible to do automatic prediction of landmark placement on DXA images with an accuracy of 0.33 mm. However, images of higher resolution would be needed to further improve the performance. Some of the landmarks used for training were inaccurate but it will not affect the performance as there were too few images to make a difference. It can also be said that augmenting the images would need to be further investigated in regards to improving the accuracy.

5.1.2 Limitations and Future perspectives

There are several limitations affecting the performance of ML-morph when automatically detecting anatomical landmarks. One discussed previously is the resolution of the images. A higher resolution would give more space for error and could make predictions closer to the truth. It was hard to distinguish the femur from the pelvis in the DXA images used and ML-morph thus had to depend on the spacing of the landmarks in the training data. This can pose a problem as the final application is to use it on pathological anatomies. Another limitation is that ML algorithms cannot learn something that it is not explicitly taught, and it can not make connections on its own. If there are errors in the placement of the manually annotated landmarks, the ML algorithm will make the same error. Using a large number of images was in this thesis positive as the impact of the errors was small. Predictions of high accuracy could thus be obtained even though the manual annotations in some images were in the wrong place.

One limitation to the use of radiography images was that the number

of radiography images was much lower than the number of DXA images used. The results presented are thus slightly misleading. More accurate would be to use the same number of images of both DXA and radiography when doing the comparison. However, one interesting result from the test with radiography images was that the predictions of the DXA images became worse when mixing them and thus implying that one single trained ML algorithm for several types of 2D X-ray images of the hip might be inefficient. Another mean of error to keep in mind when working with the radiography images is the higher resolution and hence a larger error in pixels for the same deviation in the image compared to the DXA images. In spite of this, using radiography images would be highly interesting and relevant to this project as the DXA images used are from adult males while radiography is more common to assess hip deformities in children. As the final goal of the project is to use automatic landmark detection to reconstruct hip joints of children, using radiography images would need further testing and development.

One downside to the DXA images used is that they are of hips with no history of hip deformities. Investigating how accurate sML-morph is when working with pathological images would thus be important. When training ML algorithms for pathological hips there are several possible approaches. Either there could be several specialized ones based on different abnormalities, or there could be one that is very robust and can predict the landmark positions in several types of abnormalities. Another thing to take into consideration is if images of hips from people of different stages of life should be trained together or separately. These are all possible developments of the project that would be worth investigating.

Only two ML algorithms for automatic landmark detection were tested in this thesis, oML-morph and sML-morph. There are plenty of other similar algorithms using other methods of ML to process images, a selection was presented in chapter 2.5.3. Investigating additional ML algorithms and comparing those results with the results from this thesis could be an interesting approach for the future.

5.2 CT-based FE model of the hip joint

The FE models of the hip joint were developed to model the hip cartilage contact using a subject-specific geometry from a CT image. Models of two loading scenarios, one leg standing and walking, were developed.

Models using different material parameters, constraints, and ligaments were made to find the best solution for this application.

5.2.1 One leg standing

The one leg standing model was developed as a simple model of a common loading scenario in everyday life. When using two types of constraints (rigid body or tie), it was possible to evaluate how the model was affected by including deformable bones. As seen in table 4.6, there was a large difference in the run time between the two models, using tie constraints (model 2) took 54% longer to run. However, the difference in the maximum contact pressure, the maximum von Mises stress, and the maximum major principal strain was not as prominent between the models. Using rigid body constraints was the preferred option for this application.

Model 1A-1D was used to evaluate how the different material parameters for cartilage affected the results. As presented in table 4.7, the maximum contact pressure, the maximum von Mises stress, and the maximum major principal strain were all changing as the stiffness of the cartilage increased. The maximum contact pressure in model 1D was only 3.6% higher than in model 1A. However, figure 4.5 showed a notable change in the contact pattern in the acetabular cartilage when the cartilage stiffness increased. A previous FE model of the hip cartilage contact by Li et al. that modeled one leg standing using a load of 2130 N, resulted in a maximum contact pressure of 2.7-4.1 MPa [65]. In comparison with that, the maximum contact pressure using all four sets of material parameters gave results that were only 5.2-8.5% lower. The higher maximum contact pressure in the FE model by Li et al. is reasonable since the load used was higher than the one used in this thesis.

The results for the one leg standing models using different material parameters made it difficult to conclude what parameters for cartilage were the most suitable. The maximum contact pressure was similar for all models and agreed well with the FE model by Li et al. The maximum von Mises stress (18% lower in model 1D compared to 1A) and the maximum major principal strain (63% lower in model 1D compared to 1A) varied more between the models. Due to the lack of previous FE models of the hip joint that presented the von Mises stress and the major principal strain in the hip joint cartilage, they could not be used

to evaluate the material parameters.

In conclusion, the one leg standing models showed that the rigid body constraint was the preferable option to use. It also showed that it was difficult to select suitable material parameters for cartilage by only modeling one leg standing.

5.2.2 Walking

To further develop the FE model of the hip joint cartilage contact, the load and the flexion/extension angle of the gait cycle were included. The focus of these models was to further evaluate the four options of material parameters used for cartilage and investigate how including ligaments affects the model.

That the maximum values of the contact pressure in the models using different material parameters (model 3A-3D) were observed at the first peak of the load curve (see table 4.8) was expected since that is the time point of the gait cycle where the applied load is the largest (see figure 3.12). At mid-stance, the maximum contact pressure had decreased for all models, which also is reasonable since the load was lower. At the second peak, the maximum contact pressure increased again, as expected. However, in the last time point, the swing phase, the maximum contact pressure did not follow the same pattern and it was expected to see the lowest contact pressure in the swing phase due to the low load. Instead, the maximum contact pressure was higher than at mid-stance for all models. One explanation for this can be the slightly uneven surface of the femoral head which affected the results more when the rotation angle increased.

The maximum contact pressure in the four models (3A-3D) ranged from 11.7 MPa in model 3A to 30.5 in model 3D. In previous FE models of the hip joint modeling the gait cycle by Harris et al., Anderson et al. 2008, Anderson et al. 2010, and Abraham et al., the maximum contact pressure ranged from 6.2-12.7 MPa [20, 26, 27, 28]. All the previous FE models mentioned used the load from Bergmann et al. but different weights of the subjects were used. Experimental studies had a maximum contact pressure that ranged from 9-10 MPa, measured using pressure-sensitive films [26, 27]. Out of the four sets of material parameters used for cartilage, the maximum contact pressure when using cartilage A ($D_1 = 2.043$ MPa, $C_{10} = 0.051$ MPa^{-1}) agreed the best with the previous studies. The material parameters in cartilage A were used in

the manuscript by Abraham et al. [28]. The FE model in the article by Abraham et al. had a maximum contact pressure of approximately 8 MPa, which is 31% lower than the maximum contact pressure in model 3A. The difference to the FE model by Abraham et al. can be due to several reasons, for example, that a different body weight of the subject was used, and how the geometry of the cartilage was approximated. It may also be because the thickness of the cartilage in the subject used in this thesis was thin in comparison with a healthy subject.

In the comparison of the models including ligaments (model 4 and 5) and model 3A, which did not include ligaments, some differences could be seen. The greatest difference in the translation in the center of the femoral head could be seen between the models with restricted abduction/adduction motion (model 3A and 4), and model 5 (see figure 4.11, 4.12 and 4.13). This is reasonable as more movement was allowed. It also showed that the ligaments fulfill their function to restrict movements since a model without ligaments did not complete when the abduction/adduction motion was not restricted.

To conclude the model of walking, the most suitable parameters for cartilage for this application were $D_1 = 2.043$ MPa and $C_{10} = 0.051$ MPa^{-1}, and the ligaments should be included to make the model more realistic.

5.2.3 Limitations and Future perspective

The FE model of the hip joint had several limitations that may affect the results. One of the limitations is that the labrum was not included. As mentioned in chapter 3.4.1, the labrum does not make a big difference in the load support in the hip joint. However, it still takes up some of the load and it can therefore be of interest to include it in a future FE model.

Another limitation of the model is the way the cartilages were made. Since the cartilage was segmented as the gap between the bones, and later separated into two parts, the thickness of each cartilage does not necessarily correspond to reality. To validate the simple approach for making the cartilage, a comparison to segmented cartilage from an MRI image could be made. An attempt of this was made in this thesis, using an MRI image of the same subject as in the CT image, without success. The reason for that was limited resolution and contrast in the MRI image, which was taken in 2006. It could also be of interest to use and

compare different approaches for generating the geometry and thickness of the two cartilages.

Both cartilage and bone were modeled using relatively simple material models. The FE model could be made more realistic by taking more material behaviors into account. For cartilage, a more complex material model could include the biphasic behavior of cartilage, including both the solid and fluid phases. It could also be of interest to include depth-dependent behavior. For bone, the main improvements of the model could be to include both trabecular and cortical bone. The ligaments used in the model could also be made more realistic by including the ligament pre-strain.

Evaluating whether having deformable bones would affect the result for the FE model of walking could also be of interest. When modeling standing there was no major difference between using rigid body and tie constraints except for the run time (see table 4.6). Even though the difference was small, it could also be valuable to implement deformable bone in the model of gait to further strengthen the choice of using rigid body constraints. The FE models including the gait cycle could also be made more realistic by including all movements in the hip joint (see chapter 2.1.1).

Finally, the CT image used for the subject-specific FE model was from an adult female. The goal of the project is to use the final application on children with hip deformities. Using a CT image from a child could make the model more applicable to the final application of this project since the geometry may differ. While this is true, it can be difficult to obtain CT images of children since they are more sensitive to ionizing radiation (see chapter 2.4.3).

5.3 Reconstruction of DXA images and scaling of FE model

The aim of the reconstruction and the scaling of the CT-based FE model was to present the concept of creating a FE model of the hip joint from a 2D X-ray image of the hip. This aim was fulfilled and resulted in 18 FE models based on nine reconstructed DXA images, 13 of the FE models were completed. Since the workflow to obtain the scaled FE models was executed in a relatively simple way, there were some sources of errors and limitations that needs to be addressed.

When comparing the mean cloud-to-mesh distances of reconstructions based on automatically detected landmarks and manually annotated landmarks to the FE models (table 4.11 and 4.14) it was possible to see that better predictions did not always have smaller distances. It can also be seen that in all cases where the mean distance was large (0.86 or higher), the FE model did not complete. It is not possible to find the same connection between the mean cloud-to-mesh distances of the scaled femurs (table 4.13) when comparing the models that did or did not run. Based on this, the geometrical accuracy of the 2D-to-3D reconstruction does not seem to be directly affected by the errors in landmark prediction made by sML-morph. This could be because the reconstruction algorithm is complex and based on several factors, and therefore may be influenced by more than the exact location of the landmarks. vv

When examining the cloud-to-mesh distances for the reconstructions based on automatically detected landmarks compared to the manually annotated landmarks (see figure 4.15), it is possible to see that there was no pattern to the size differences but that the largest deviations were in the femoral head. This is problematic as the femoral head is the region of highest interest to this project. The differences in the top of the greater trochanter and the lesser trochanter do not make as big of a difference as they are not as valuable in this application. In the cloud-to-mesh visualizations of the scaled femurs (see figure 4.16), there was a more clear pattern of the sizes where the femoral head was smaller in the automatically detected landmark based femurs in all but two cases. The larger deviations in the femoral head were not consistent between the reconstructed femurs and scaled femurs which shows that the scaling changed the geometry of the FE model in inconsistent ways between two reconstructions of the same image.

As the FE models did not use the reconstructed femurs but scaled a CT-based FE model to match the size, in future work, it would be of interest to use the reconstructed femur instead of a scaled version. The reason for not using the reconstructed femurs were that the reconstructions only provided the femur, and did not include the pelvis or any of the two cartilages.

The numbering of the nodes in the different reconstructed meshes were not the same and the four points used to measure the distances for scaling the FE models needed to be manually picked. This was time-consuming and could lead to faults due to human error making

the scaling a part of the thesis that could be improved. Another possible improvement is to change the measurements and nodes used for scaling or to change the method for scaling entirely. As the femoral head is the part of the femur that is of the highest interest, using more measurements of that part could give a more accurate reconstruction. One issue that was encountered was that scales were inaccurate when the measurement used was parallel to an axis. This could be addressed by possibly changing the coordinate system in the reconstructed femur or picking points on the diagonal instead of in the anterior-posterior direction. Another possible way to improve the scaling is to scale the models based on the volume. The reason this was not further investigated was that the CT-base FE model and the reconstructed femurs did not include the same amount of the proximal femur. Using volume would also scale the femur isometrically, not taking the geometry of the femur into account. Therefore, it would be hard to predict cartilage contact, especially in pathological hips. In conclusion, a better method of scaling is needed that is complex enough to take anatomical differences in both shape and size of the proximal femur into account.

The limitation of this simple approach to reconstructing, scaling, and running new FE models can especially be highlighted by studying the five FE models that did not run completely. One pattern that can be seen in table 4.12 is that the scaling factors used for the models that completed were similar in the x-, y-, and z-direction for most of the femurs. The models with errors had larger deviations in the scaling factors. One example of where both models did not complete is Best 1 where the mean cloud-to-mesh distance between the automatically annotated landmarks and the manually annotated ones is -0.47 mm. The two scaled femurs of Best 1 were very similar but did not run as the difference between the biggest and smallest ratio in the manual annotation based femur was 5 percentage points and in the predicted annotation based was 20 percentage points. In general, a difference between one axis and another larger than 11 percentage points resulted in models that did not complete. The large difference between the ratios changed the shape of the FE model in an inaccurate way, which lead to problems in the cartilage contact area. Most of the contact was close to the edges causing large distortion in the elements. The problem with the deviating ratios can either be caused by taking the wrong measurements or that the size of those reconstructed femurs differed that much from the CT-based FE model. The conclusion of this is that the scaling

makes the largest impact on weather a model completes, specifically how large the difference between the ratios in different directions is. Possible alternatives to scaling could be to use a statistical shape model or do mesh morphing.

When comparing the results for the five pairs of models that were completed (Best 3, Middle 1, Middle 2, Worst 1, and Worst 3), it was possible to see that the smallest difference in maximum contact pressure between the reconstruction based on automatically detected landmarks and manual annotations, was in the best model (Best 3), and the largest difference was seen in the worst (Worst 3) (see table 4.14). However, there was no pattern that showed that the difference was always larger for the models with less accurate predictions. More models would be necessary to compare to draw a conclusion on the performance. In figure 4.17, it can also be seen how the contact pattern in the acetabular cartilage was more similar in the models with a smaller difference in the maximum contact pressure, and vary more between the ones with a larger difference. All the models from predictions were more similar, compared to the five from manually placed landmarks. This indicates that the shape of the femoral head becomes similar in all models from predictions.

In conclusion, it is possible to make 3D FE models of the hip joint based on automatically detected landmarks in DXA images. However, the workflow requires some improvements such as exploring additional methods for scaling the model.

5.4 Future perspective

The bigger picture of this project aims to use an automatic approach to assess hip deformities in children. Using and combining the automatic landmark detection and the CT-based FE model requires manual work. In future work, this requires improvements to make it more automatic and to remove the sources of error mentioned in each section. Improving these tools and making the process more automatic would make it possible to evaluate hip deformities in children using images that are already being captured without exposing them to additional radiation. It could also give a better understanding of the link between hip deformities and OA progression.

5.5 Ethics

All the clinical images used in this thesis came from earlier performed studies and were therefore not collected for this specific project. This means that no subjects were exposed to additional radiation due to this thesis.

This project would enable modeling of the hip cartilage contact in children with pediatric hip deformities based on 2D X-ray images. As the images are already used for diagnosing, no additional radiation exposure would be needed. This project would thus gain the patient and medical professional valuable information about the state of the disease, without further tests or radiation exposure. This is especially valuable for children as they are more sensitive to radiation.

The methodologies investigated in this thesis would need additional evaluation to be ready for clinical implementation. The ambition is that this tool can be used to predict the effects hip deformities have on the cartilage and thus limit the risk for osteoarthritis as well as unnecessary intervention. But what if the tool suggests unnecessary intervention? Machine learning or a tool based on numerical modelling should never replace a knowledgeable professional but be used as a tool in addition to the evaluations done today to make an educated diagnosis. In addition, a limitation to ML and numerical modelling is that it only knows what it has been told. This tool would be based on a single 2D X-ray image of the patient and do not take other aspects of the patients life and circumstance into consideration, something that is of importance when making a diagnosis. However, if the method could assess the risk of developing osteoarthritis, it could be valuable in the eyes of both the patient and the welfare system. It could contribute to higher well-being for children with hip deformities through several stages of their life.

Chapter 6

Conclusions

During this thesis, methods for automatic landmark detection were evaluated, a subject-specific FE model of the hip joint was developed, and the two parts were combined to create a FE model based on a 2D X-ray image of the hip. This was done using a previously developed reconstruction algorithm based on anatomical landmarks to present a concept of a tool that can use DXA images to create a 3D FE model of the hip joint cartilage. The main conclusions that could be drawn were:

- Performing automatic landmark detection on DXA gave predictions with an average accuracy of 0.33 mm per landmark in images with a resolution of 1.05 mm per pixel in the x-direction and 0.60 mm per pixel in the y-direction. The sML-morph predictions were of high enough accuracy to be used by the reconstruction algorithm without major differences. To further improve the accuracy of sML-morph, images of higher resolution would be needed.

- The CT-based FE model can be used to predict the hip cartilage contact in two common loading scenarios, one leg standing and walking. The most suitable material parameters for cartilage when using a neo-Hookean hyperelastic material were $C_{10} = 2.043$ MPa and $D_1 = 0.051$ MPa^{-1} and it was not necessary for the model to have deformable bones. The ligaments of the hip joint capsule were included to make the FE model more realistic. Future work could include the use of a more complex material model.

- It was possible to reconstruct femurs based on the automatically detected landmarks in DXA images and scale the FE model of the

hip joint to obtain a subject-specific size. The scaling had several limitations that in the future need to be improved.

Finally, the developed tool that uses automatic landmark detection of DXA images to model the hip cartilage contact using numerical methods can potentially give valuable information regarding the connection between hip abnormalities in children and OA progression. Combining the FE model of the hip joint with reconstructions of the femur based on predicted anatomical landmarks is a promising method but needs further development to be clinically applicable.

Bibliography

[1] Mayo Clinic Staff. Osteoarthritis, 06 2021. https://www.mayoclinic.org/diseases-conditions/osteoarthritis/symptoms-causes/syc-20351925. [Online; accessed 2022-03-28].

[2] S. Pun. Hip dysplasia in the young adult caused by residual childhood and adolescent-onset dysplasia. *Current reviews in musculoskeletal medicine*, 9(4):427–434, 12 2016.

[3] M. G. Wadström, N. P. Hailer, and Y. D. Hailer. No increased mortality after total hip arthroplasty in patients with a history of pediatric hip disease: a matched, population-based cohort study on 4,043 patients. *Acta orthopaedica*, 92(6):673–677, 12 2021.

[4] Q. Li, K. Amano, T. M. Link, and C. B. Ma. Advanced imaging in osteoarthritis. *Sports health*, 8(5):418–428, 09 2016.

[5] S. Yang, N. Zusman, E. Lieberman, and R. Y. Goldstein. Developmental Dysplasia of the Hip. *Pediatrics*, 143(1), 01 2019.

[6] Pulmonary Associates of Brandon. What's the difference between A chest X-Ray and A chest CT scan?, 2017. https://floridachest.com/pulmonary-blog/chest-x-ray-chest-ct-scan-differences. [Online; accessed 2022-05-26].

[7] National institute of health. Computed tomography (CT), 12 2019. https://www.nibib.nih.gov/sites/default/files/2020-06/Computed_Tomography_Fact_Sheet.pdf. [Online; accessed 2022-03-28].

[8] S. P. Väänänen, L. Grassi, G. Flivik, J. S. Jurvelin, and H. Isaksson. Generation of 3d shape, density, cortical thickness and finite element mesh of proximal femur from a dxa image. *Medical Image Analysis*, 24(1):125–134, 2015.

[9] M. Gold, A. Munjal, and M. Varacallo. Anatomy, bony pelvis and lower limb, hip joint. In *StatPearls*. StatPearls Publishing, Treasure Island (FL), 01 2022.

[10] M. Funiciello. Hip anatomy, 08 2011. `https://www.arthritis-health.com/types/joint-anatomy/hip-anatomy`. [Online; accessed 2022-03-28].

[11] A. Mauldin. Anatomical position. `https://www.osmosis.org/answers/anatomical-position`. [Online; accessed 2022-03-28].

[12] The figure was partly generated using Servier Medical Art provided by Servier, licensed under a Creative Commons Attribution 3.0 unported license. `smart.servier.com`.

[13] O. Jones. Anatomical terms of movement. `https://teachmeanatomy.info/the-basics/anatomical-terminology/terms-of-movement/`. [Online; accessed 2022-05-02].

[14] E. F. Morgan, G. U. Unnikrisnan, and A. I. Hussein. Bone mechanical properties in healthy and diseased states. *Annual Review of Biomedical Engineering*, 20(1):119–143, 06 2018.

[15] R. B. Martin, N. A. Sharkey, and D. B. Burr. *Skeletal Tissue Mechanics*. Springer-Verlag, 1998.

[16] C. Figueroa and P. H. Le. Anatomy, bony pelvis and lower limb, pelvis bones. In *StatPearls*. StatPearls Publishing, Treasure Island (FL), 01 2022.

[17] A. Chang, G. Breeland, and J. B. Hubbard. Anatomy, bony pelvis and lower limb, femur. In *StatPearls*. StatPearls Publishing, Treasure Island (FL), 01 2022.

[18] J. Van Houcke, E. A. Audenaert, P. R. Atkins, and A. E. Anderson. A combined geometric morphometric and discrete element modeling approach for hip cartilage contact mechanics. *Frontiers in Bioengineering and Biotechnology*, 8, 04 2020.

[19] C. R. Henak, G. A. Ateshian, and J. A. Weiss. Finite element prediction of transchondral stress and strain in the human hip. *Journal of biomechanical engineering*, 136, 11 2013.

[20] M. D. Harris, A. E. Anderson, C. R. Henak, B. J. Ellis, C. L. Peters, and J. A. Weiss. Finite element prediction of cartilage contact stresses in normal human hips. *Journal of orthopaedic research : official publication of the Orthopaedic Research Society*, 30:1133–1139, 07 2012.

[21] J. Bergström. Elasticity/hyperelasticity. In *Mechanics of Solid Polymers*, pages 209–307. William Andrew Publishing, 07 2015.

[22] C. R. Henak, A. E. Anderson, and J. A. Weiss. Subject-Specific Analysis of Joint Contact Mechanics: Application to the Study of Osteoarthritis and Surgical Planning. *Journal of Biomechanical Engineering*, 135(2), 02 2013.

[23] A. J. S. Fox, A. Bedi, and S. A. Rodeo. The basic science of articular cartilage: Structure, composition, and function. *Sports Health*, 1(6):461–468, 11 2009.

[24] R. Glenister and S. Sharma. Anatomy, bony pelvis and lower limb, hip. In *StatPearls*. StatPearls Publishing, Treasure Island (FL), 01 2022.

[25] A. H. Spannow, M. Pfeiffer-Jensen, N. T. Andersen, T. Herlin, and E. Stenbøg. Ultrasonographic measurements of joint cartilage thickness in healthy children: Age- and sex-related standard reference values. *The Journal of Rheumatology*, 37(12):2595–2601, 12 2010.

[26] A. E. Anderson, B. J. Ellis, S. A. Maas, C. L. Peters, and J. A. Weiss. Validation of finite element predictions of cartilage contact pressure in the human hip joint. *Journal of biomechanical engineering*, 130, 10 2008.

[27] A. E. Anderson, B. J. Ellis, S. A. Maas, and J. A. Weiss. Effects of idealized joint geometry on finite element predictions of cartilage contact stresses in the hip. *Journal of Biomechanics*, 43(7):1351–1357, 05 2010.

[28] C. L. Abraham, S. A. Maas, J. A. Weiss, B. J. Ellis, C. L. Peters, and A. E. Anderson. A new discrete element analysis method for predicting hip joint contact stresses. *Journal of biomechanics*, 46:1121–1127, 04 2013.

[29] M. Smith. *ABAQUS/Standard User's Manual, Version 6.10*. Dassault Systèmes Simulia Corp, United States, 2010.

[30] M. K. Mulcahey and J. W. T. Byrd. Femoroacetabular impingement, 08 2020. https://orthoinfo.aaos.org/en/diseases--conditions/femoroacetabular-impingement/. [Online; accessed 2022-03-23].

[31] Mayo clinic staff. Legg-Calve-Perthes disease, 06 2020. https://www.mayoclinic.org/diseases-conditions/legg-calve-perthes-disease/symptoms-causes/syc-20374343. [Online; accessed 2022-03-28].

[32] D. Peck. Slipped capital femoral epiphysis: diagnosis and management. *Am. Fam. Physician*, 82(3):258–262, 08 2010.

[33] W. C. Shiel Jr. Osteoarthritis (OA or degenerative arthritis), 02 2021. https://www.medicinenet.com/osteoarthritis/article.htm. [Online; accessed 2022-03-28].

[34] National institute of health. X-ray, 11 2019. https://www.nibib.nih.gov/sites/default/files/2020-06/X-ray_Fact_Sheet.pdf. [Online; accessed 2022-03-28].

[35] S.-J. Lim and Y.-S. Park. Plain radiography of the hip: A review of radiographic techniques and image features. *Hip and pelvis*, 27(3):125–134, 09 2015.

[36] A. El Maghraoui and C. Roux. DXA scanning in clinical practice. *QJM: An International Journal of Medicine*, 101(8):605–617, 03 2008.

[37] Svenska Osteoporossällskapet. Vad är DXA. Online, 12 2021. https://svos.se/bentathetsmatning/vad-ar-dxa/. [Online; accessed 2021-05-17].

[38] C. Land. Ionizing radiation, 09 2019. https://www.britannica.com/science/ionizing-radiation. [Online; accessed 2022-05-10].

[39] F. Chollet. *Deep Learning with Python*. Manning Publications Co., Shelter Island, USA, 2018.

[40] A. Porto and K. Voje. Ml-morph: A fast, accurate and general approach for automated detection and landmarking of biological structures in images. *Methods in Ecology and Evolution*, 11, 02 2020.

[41] T. Shah. About train, validation and test sets in machine learning. `https://tarangshah.com/blog/2017-12-03/train-validation-and-test-sets/`. [Online; accessed 2022-05-29].

[42] V. L. Le. *Automatic landmarking for 2D biological images : image processing with and without deep learning methods*. PhD thesis, Université de Bordeaux, 11 2019.

[43] K. Satyam. 5 techniques to work with imbalanced data in machine learning, 09 2021. `https://towardsdatascience.com/5-techniques-to-work-with-imbalanced-data-in-machine-learning-80836d45d30c`. [Online; accessed 2022-04-11].

[44] N. Dalal and B. Triggs. Histograms of oriented gradients for human detection. In *2005 IEEE Computer Society Conference on Computer Vision and Pattern Recognition (CVPR'05)*, volume 1, pages 886–893 vol. 1, 2005.

[45] R. C. Steorts. Tree based methods: Regression trees, 2017. `https://www2.stat.duke.edu/~rcs46/lectures_2017/08-trees/08-tree-regression.pdf`. [Online; accessed 2022-05-17].

[46] I. Goodfellow, Y. Bengio, and A. Courville. *Deep Learning*. MIT Press, 2016. `http://www.deeplearningbook.org`.

[47] S. Bej, N. Davtyan, M. Wolfien, M. Nassar, and O. Wolkenhauer. Loras: an oversampling approach for imbalanced datasets. *Machine Learning*, 110(2):279–301, 02 2021.

[48] A. Silberschat, P. B. Galvin, and G. Gagne. *Operating System Concepts*. John Wiley and Sons Inc, 8 edition, 2009.

[49] A. Porto. simple-ml-morph, 05 2021. `https://github.com/agporto/simple-ml-morph`.[Online; accessed 2022-05-04].

[50] V.-L. Le, M. Beurton-Aimar, A. Zemmari, and N. Parisey. Landmarks detection by applying deep networks. In *2018 1st International Conference on Multimedia Analysis and Pattern Recognition (MAPR)*, pages 1–6. IEEE, 2018.

[51] S. Mehryar, K. Martin, K. N. Plataniotis, and S. Stergiopoulos. Automatic landmark detection for 3d face image processing. In *IEEE Congress on Evolutionary Computation*, pages 1–7, 2010.

[52] C. A. Manacorda and S. Asurmendi. Arabidopsis phenotyping through geometric morphometrics. *GigaScience*, 7(7), 06 2018.

[53] N. Saabye Ottosen and H. Petersson. *Introduction to the finite element method*. Prentice Hall, New York, 1992.

[54] Abaqus Unified FEA - SIMULIA™ by Dassault Systèmes®, 2020. `https://www.3ds.com/products-services/simulia/products/abaqus/`.

[55] D. Mellström, O. Johnell, O. Ljunggren, A. L. Eriksson, M. Lorentzon, H. Mallmin, A. Holmberg, I. Redlund-Johnell, E. Orwoll, and C. Ohlsson. Free testosterone is an independent predictor of bmd and prevalent fractures in elderly men: Mros sweden. *Journal of Bone and Mineral Research*, 21(4):529–535, 04 2016.

[56] Center for Artificial Intelligence in Medicine Chang Gung Memorial Hospital. Pelvis-X-ray_Segmentation_Database, 08 2020. `https://github.com/cgmhaicenter/Pelvis-X-ray_Segmentation_Database`. [Online; accessed 2022-04-19].

[57] D. Testi, P. Quadrani, and M. Viceconti. Physiomespace: digital library service for biomedical data. *Philosophical Transactions of the Royal Society A: Mathematical, Physical and Engineering Sciences*, 368(1921):2853–2861, 2010.

[58] G. Bradski and A. Kaehler. *Learning OpenCV: Computer Vision in C++ with the OpenCV Library*. O'Reilly Media, Inc., 2nd edition, 2013.

[59] A. Fedorov, R. Beichel, J. Kalpathy-Cramer, J. Finet, J.-C. Fillion-Robin, S. Pujol, C. Bauer, D. Jennings, F. M. Fennessy, M. Sonka, J. Buatti, S. R. Aylward, J. V. Miller, S. Pieper, and R. Kikinis. 3D Slicer as an Image Computing Platform for the Quantitative Imaging Network. *Magn Reson Imaging*, 30(9), 07 2012. `https://www.slicer.org/`.

[60] J. Li, T. D. Stewart, Z. Jin, R. K. Wilcox, and J. Fisher. The influence of size, clearance, cartilage properties, thickness and hemiarthroplasty on the contact mechanics of the hip joint with biphasic layers. *Journal of biomechanics*, 46(10):1641–1647, 06 2013.

[61] C. R. Henak, B. J. Ellis, M. D. Harris, A. E. Anderson, C. L. Peters, and J. A. Weiss. Role of the acetabular labrum in load support across the hip joint. *Journal of Biomechanics*, 44(12):2201–2206, 08 2011.

[62] J. Li, X. Hua, Z. Jin, J. Fisher, and R. K. Wilcox. Biphasic investigation of contact mechanics in natural human hips during activities. *Proc Inst Mech Eng H*, 228(6):556–563, 06 2014.

[63] Autodesk Inc. Autodesk meshmixer. `https://www.meshmixer.com/`. [Online; accessed 2022-03-29].

[64] P. Cignoni, M. Callieri, M. Corsini, M. Dellepiane, F. Ganovelli, and G. Ranzuglia. Meshlab: an open-source mesh processing tool. volume 1, pages 129–136, 01 2008.

[65] J. Li, T. D. Stewart, Z. Jin, R. K. Wilcox, and J. Fisher. The influence of size, clearance, cartilage properties, thickness and hemiarthroplasty on the contact mechanics of the hip joint with biphasic layers. *Journal of Biomechanics*, 46(10):1641–1647, 06 2013.

[66] Altair Engineering Inc. Hypermesh 2021. `https://www.altair.com/hypermesh/`.

[67] P. Bolcos. Meshing complex geometries in abaqus, 10 2021. `https://info.simuleon.com/blog/hexahedral-meshes-for-complex-geometries-in-abaqus`. [Online; accessed 2022-02-22].

[68] A. H. Aitkenhead. STL to ACIS SAT conversion, 05 2021. `https://se.mathworks.com/matlabcentral/fileexchange/27174-stl-to-acis-sat-conversion`. [Online; accessed 2022-02-22].

[69] D. L. Robinson, M. E. Kersh, N. C. Walsh, D. C. Ackland, R. N. de Steiger, and M. G. Pandy. Mechanical properties of normal and osteoarthritic human articular cartilage. *Journal of the Mechanical Behavior of Biomedical Materials*, 61:96–109, 08 2016.

[70] M. C. M. Fischer, S. A. G. A. Grothues, J. Habor, M. de la Fuente, and K. Radermacher. A robust method for automatic identification of femoral landmarks, axes, planes and bone coordinate systems using surface models. *Scientific reports*, 10(1):20859, 11 2020.

[71] G. Wu, S. Siegler, P. Allard, C. Kirtley, A. Leardini, D. Rosenbaum, M. Whittle, D. D. D'Lima, L. Cristofolini, H. Witte, O. Schmid, and I. Stokes. Isb recommendation on definitions of joint coordinate system of various joints for the reporting of human joint motion—part i: ankle, hip, and spine. *Journal of Biomechanics*, 35(4):543–548, 04 2002.

[72] G. Bergmann, G. Deuretzbacher, M. Heller, F. Graichen, A. Rohlmann, J. Strauss, and G. N. Duda. Hip contact forces and gait patterns from routine activities. *Journal of Biomechanics*, 34(7):859–871, 07 2001.

[73] C. L. Lewis, S. A. Sahrmann, and D. W. Moran. Effect of hip angle on anterior hip joint force during gait. *Gait and Posture*, 32(4):603–607, 10 2010.

[74] Z. Zou, A. Chávez-Arreola, P. Mandal, T. N. Board, and T. Alonso-Rasgado. Optimization of the position of the acetabulum in a ganz periacetabular osteotomy by finite element analysis. *Journal of Orthopaedic Research*, 31(3):472–479, 10 2013.

[75] D. Girardeau-Montaut. CloudCompare - open source project. `http://www.cloudcompare.org/`. [Online; accessed 2022-05-27].

[76] CloudCompare wiki. Cloud-to-mesh distance. `https://www.cloudcompare.org/doc/wiki/index.php/Cloud-to-Mesh_Distance`. [Online; accessed 2022-05-29].